ANALYSIS OF COULOMB EXCITATION DATA FROM IUAC

Version 12/11/09

Rakesh Kumar[1], S. Muralithar[1], R.P. Singh[1], A.Jhingan[1], S.K. Mandal[2], S.C. Pancholi[1], P. Doomenbal[3], J. Gerl[3], R. Bhowmik ,H.J. Wollersheim[3]

[1]IUAC [2] Delhi University [3]GSI

EXPERIMENTAL SETUP

In the experiment carried out at IUAC, targets of ^{112}Sn & ^{116}Sn were bombarded with ^{58}Ni beam at 175 MeV. Both the targets were of thickness ~0.53 mg/cm^2 with an enrichment of 99.5% and 98%, respectively. The scattered beam and recoils were detected in an annular PPAC (11cm from target), subtending the angular range 15°- 45° in the forward direction. The cathode of the PPAC was subdivided into 20 segments for ϕ measurement. The anode of the PPAC was subdivided into annular strips of constant tanθ, and delay line readout from both ends was used to measure θ information. The γ-rays from Coulomb excitation of Ni and Sn were detected in four clover detectors mounted at $\theta_\gamma \sim 135°$ with respect to the beam axis (distance to target 22±2cm). The ϕ-angles for the clovers were ±55° and ±125° with respect to the vertical direction. The γ-events in coincidence with the PPAC cathode signals were recorded event by event.

During the experiment, the 16 energies from the 4 segmented clover detectors, four timing from the clovers, 20 timing signals from individual front PPAC detectors, and four signals from the two ends of the delay lines were recorded event by event. To avoid any systematic error due to instrumental drift, runs from ^{112}Sn and ^{116}Sn targets, each of ~ 3 hour duration, were interspersed alternatively. Energy and efficiency calibration run for the clover detectors was carried out at the end using a ^{152}Eu source. A block diagram of the experimental setup is shown below.

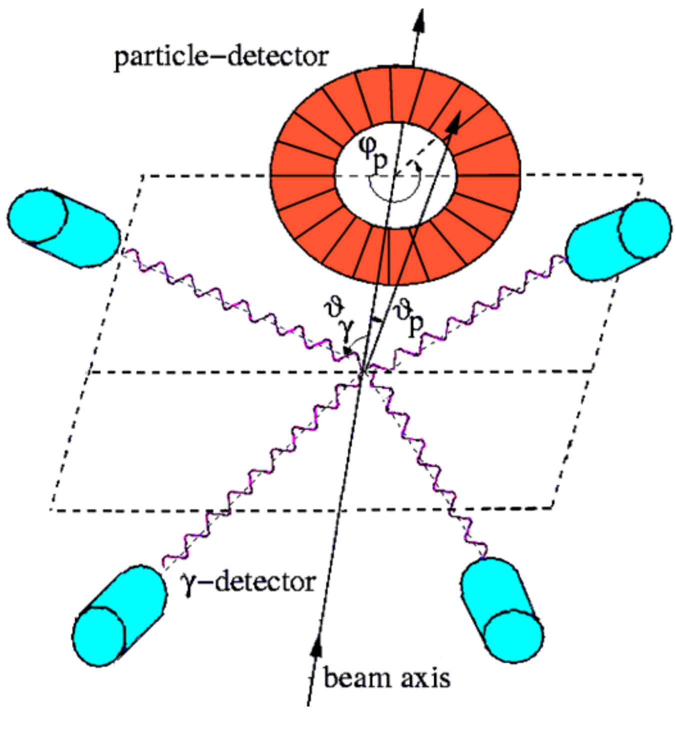

Fig.1: Experimental setup for Coulomb excitation measurements. Four clover detectors were placed at $\theta_\gamma \sim 135°$ and $\phi_\gamma \sim \pm 55°$ & $\pm 125°$ with respect to the beam direction.

DATA ANALYSIS

The standard ***INGASORT*** analysis package was modified to incorporate the additional signals obtained from the Coulomb excitation experiment. The command ***PPAC*** gave information about the ϕ-angle (ranging from 1-20) depending on which PPAC TAC was non-zero and also identified multi-hit events. Multi-hit events (cross talk between neighbouring ϕ-segments) were less than 5% of the total events. In the present experiment only one reaction partner could be measured at a given time, either the scattered projectile or the recoil nucleus (see fig.2). The existing ***TDC*** command could identify which pair of delay line signals had data and determined the time difference between them. ***CLOVER*** command was used to match amplifier gains and provided the add-back energies of the clover detectors. In addition, it identified which of the segments had data allowing for segment-wise Doppler correction. The Doppler correction was incorporated in the ***USER*** command that used information from the clover angles (θ_γ, ϕ_γ) and the PPAC signals (θ_p, ϕ_p) computed from the input data.

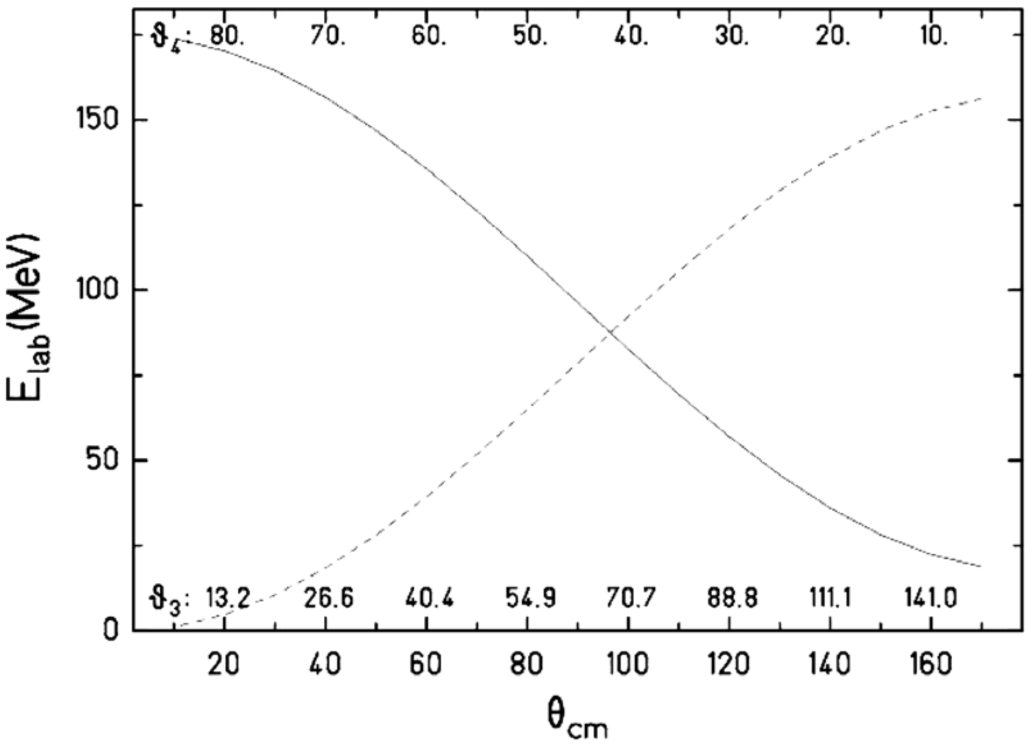

Fig.2: Kinematics for Coulomb excitation experiment: θ_3 is the lab angle of the projectile and θ_4 is the lab angle of the target nucleus. The PPAC detector spanned a range of 15° to 45° in the laboratory.

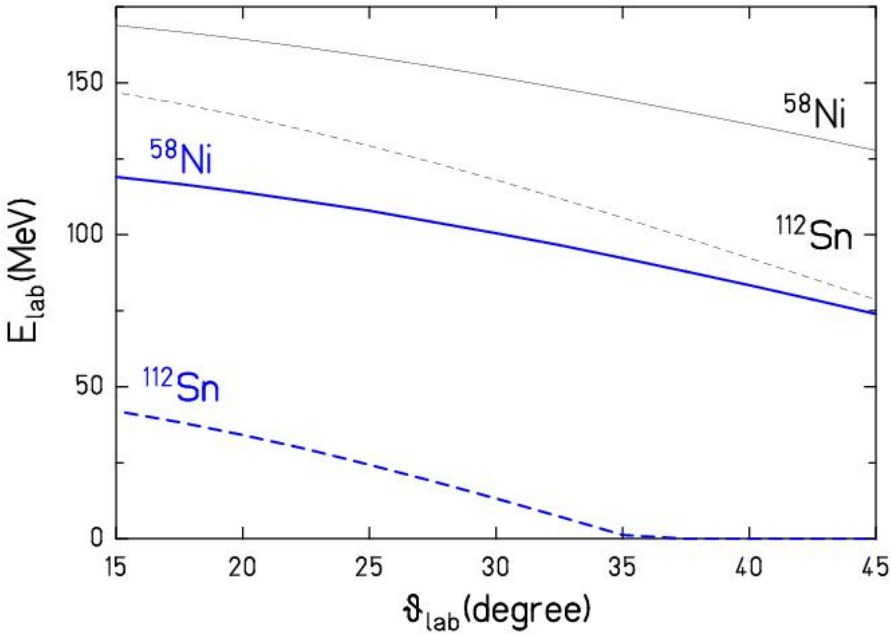

Fig.2a: Energies of the ^{58}Ni projectiles and ^{112}Sn recoils versus the lab angles ϑ_3 and ϑ_4 for the angular range of 15° to 45° covered by the PPAC. The black lines (full and dashed for ^{58}Ni and ^{112}Sn, respectively) are taken from fig.2, while the blue lines (full and dashed for ^{58}Ni and ^{112}Sn, respectively) are corrected for the energy loss in 10µm MYLAR foil, which was used as an entrance window of the PPAC.

Fig.2a shows the kinetic energies of the ^{58}Ni projectiles and ^{112}Sn recoils (based on kinematical calculations, see fig.2) for the angular range of 15° to 45° covered by the PPAC. Due to the use a rather thick entrance window (10µm MYLAR, ρ=1.39 g/cm^3) for the PPAC, the detected kinetic energies of the ^{58}Ni projectiles and ^{112}Sn recoils are much lower (see fig2a: blue lines). The energy loss in MYLAR was taken from Northcliff & Schilling (Nucl. Data Tables A7, 1970, p.233). It would be seen in the next section that the fast cathode signals in the PPAC for both groups of particles were sufficiently large to trigger the timing electronics for PPAC. The corresponding slower anode signal for the recoiling ^{112}Sn nuclei, which is used for delayline readout of the angle (θ) information, was however below the detection threshold. In this way close collision (θ_{cm} = 90^0-150^0) events are not considered in the present measurement.

Fig 3a shows the add-back energy spectrum from one of the clover detectors in coincidence with the PPAC detectors. Six broad peaks (three each in the vicinity of 1.2 and 1.4 MeV) could be identified. From kinematics (table I), they can be identified as projectile excitation (~ 1.4 MeV) & target excitation (~ 1.2 MeV) for values ϕ_{12} ranging between 0° and 180° where $\phi_{12} = |\phi_\gamma - \phi_p|$. From phase space consideration ($|dE_\gamma/d\phi|$ is minimum for ϕ ~ 0° and 180°), one expects to see peaks at E_γ = 1200, 1233 &1264 keV corresponding to ^{112}Sn and at 1350, 1413 & 1495 keV corresponding to ^{58}Ni excitation. For particles (Ni or Sn) detected on the same side as the gamma detector, both of the recoil-shifted energies would be similar in value. For a given ϕ, there would be a pair of peaks of similar energies (arising from projectile or target excitation) the splitting between whom would be maximum at ϕ=180°, merging to each other at ϕ = 0°. As a result, identification of the type of particle detected in the PPAC would be required for good Doppler correction.

Table I

Energies of the Doppler shifted γ-rays in keV

PPAC signal	ϕ_{12}	Ni excitation	Sn excitation
Nickel detected	0	1413	1233
	90	1381	1249
	180	1350	1264
Sn detected	0	1410	1235
	90	1451	1217
	180	1495	1200

θ_γ = 144° θ_p = 30° E^o_{Ni} = 1454 keV E^o_{Sn} = 1257 keV

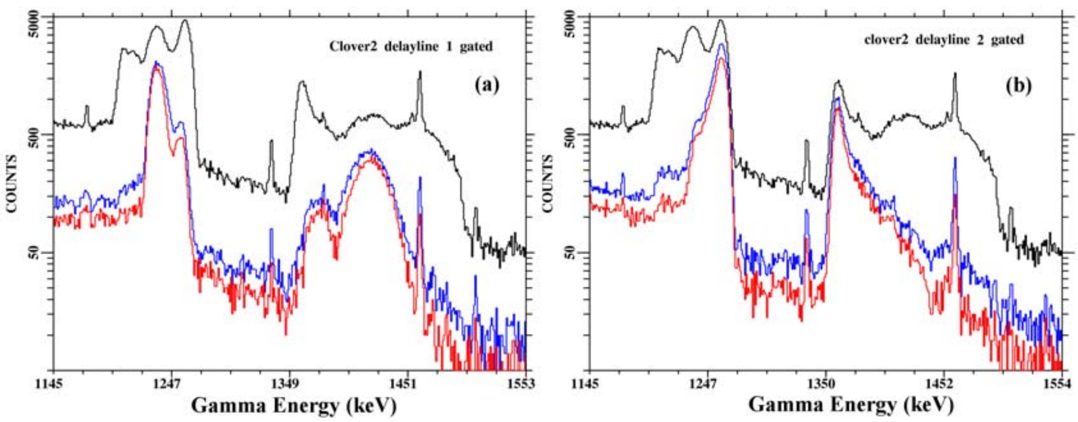

Fig.3: Ungated addback spectrum for clover 2 (black) and addback spectra gated by (a) left delay line and (b) right delay line. The spectra in coincidence with the small angle end of the delay line (inner contact readout) are plotted in blue while the spectra in coincidence with the large angle end of the delay line (outer contact readout) are plotted in red.

The slowed-down Sn recoil nuclei could be measured with the ϕ-segments but not with the delay-line (energy signals one order of magnitude smaller). For the left delay-line the Sn excitation occurs at ~1234 keV and the Ni excitation at ~1405 keV. In addback spectrum of clover 2 (fig 3) the Sn excitation shows up at 1245-1261 keV and the Ni excitation at 1350-1382 keV, when gated on the right delay-line. (see Appendix III).

From the energy data from individual segments, the addback factor could be determined (INGA command *area* or *fit*). For Clover-3 (see table II below), the addback factor for ^{112}Sn excitation was determined to be ~ 1.50 by the ratio of clover counts relative to the sum of the counts in the individual crystals. (To reduce background, the analysis was done for the Doppler-corrected peaks.)

Table II

Addback Ratio for Clover Detectors

Crystal No.	COUNTS	
	^{112}Sn excitation	Ni excitation
1	11550 ± 523	4864 ± 247
2	12430 ± 206	5049 ± 173
3	10577 ± 173	4358 ± 125
4	9891 ± 186	4064 ± 144
ADD BACK	67111 ± 523	18020 ± 623

A time-of-flight spectrum was generated between the γ-signal from the Clover detectors and timing from the PPAC detectors. The method of analysis is described in detail in appendix 1. The centroids for the detected Ni peaks for different ϕ segments were matched within ± 10 channels (1ns). Fig 4 shows the time of flight spectra for Clover detector with respect to PPAC detectors gated by different energy windows in the clover detector. The T-O-F difference between the projectile-like (fig 4a, gate on 1264 keV Ni detected in PPAC) and target-like fragments (fig 4b, gate on 1200 keV Sn detected in PPAC) was found to be small compared to the timing resolution of the clover detectors. As a result, the T-O-F information could be used only to separate the 'random' events from the 'true' coincidences.

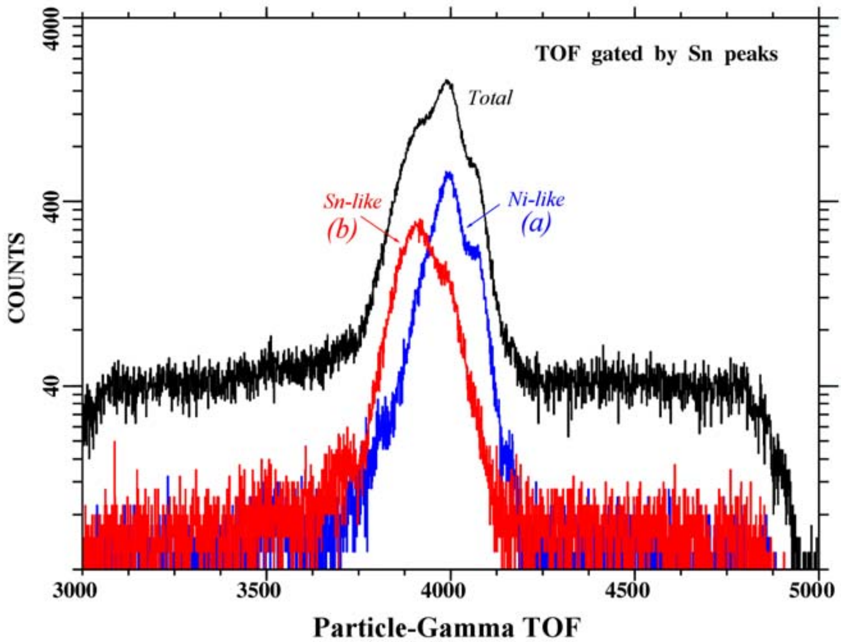

Fig.4: Gamma-particle time-of-flight spectrum (black) and γ-energy gated spectra for Ni (blue) or Sn (red) particles detected in PPAC.

The events associated with 'random' coincidence between the γ-rays in the Clover detectors and the particles detected in the PPAC were typically less than 1% of the 'prompt' events. Fig 5 shows the γ-spectra for random events (bottom curve) and the background-subtracted prompt events (top curve). As expected, the discrete γ-transitions seen in background spectrum disappear in the prompt peak.

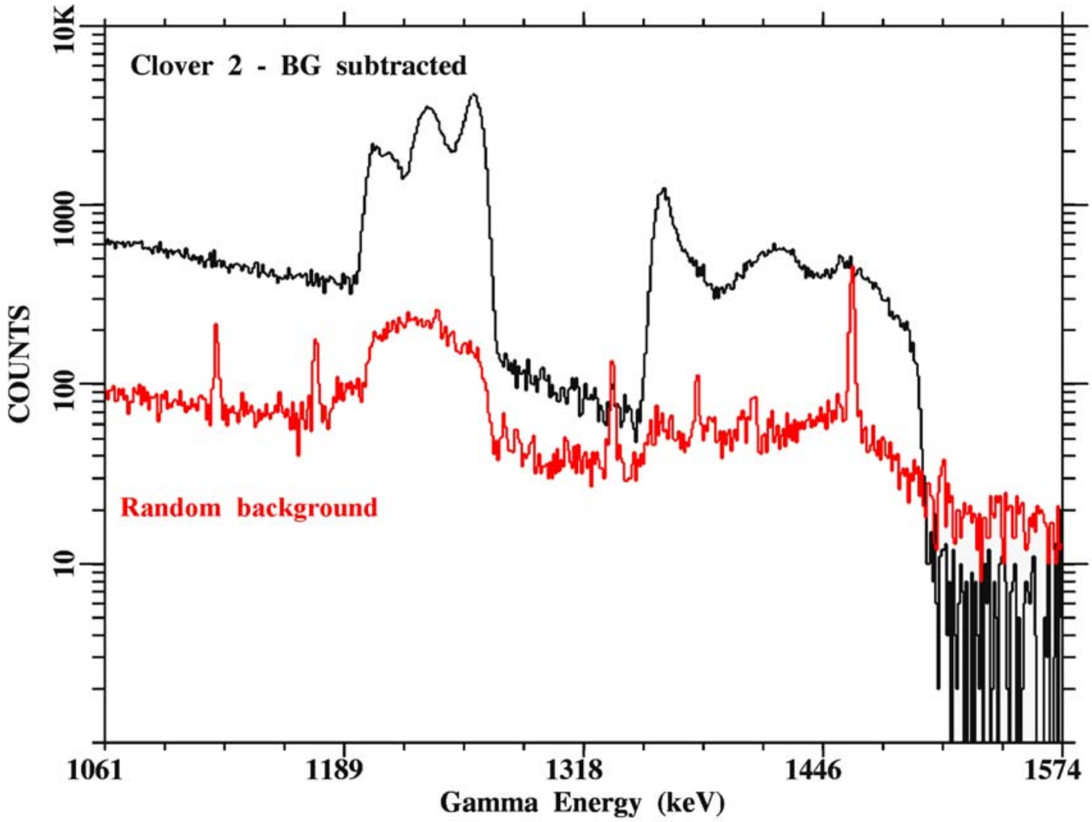

Fig.5: γ-spectra associated with the random events (red curve) and background-subtracted prompt spectrum (top curve)

For the angle readout, four signals were recorded from the two ends of the right and left delay lines. The θ information can be obtained by two different methods (i) from the difference in times between the inner and outer edges of the delay lines (DDL = $t_{inner} - t_{outer}$) and (ii) the difference in time between either of the readouts and the timing derived from the cathode signals recorded for individual ϕ segments (SDL = t_{inner} - $t_{cathode}$) During data collection, some of the segments showed lower count rates compared to the other segments (fig 6). The slow delay line signals were a factor of ten lower in amplitude compared to the fast cathode signals and showed a strong position dependent attenuation. In addition, the events associated with the detection of Sn-like particles in the PPAC were almost completely suppressed in the delay line-gated spectra. As a result, the count rates recorded by the inner (blue curve) and the outer edge (red curve) were a factor of 2 - 4 lower compared to the raw PPAC signals.

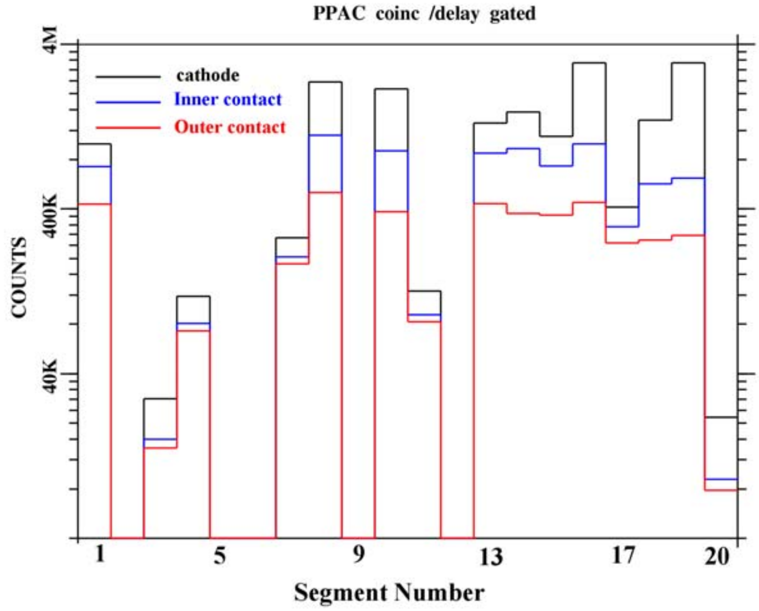

Fig 6. Total number of counts recorded for each PPAC segment during the γ-p coincidence run (black curve). The blue and red curves show the corresponding counts in coincidence with signals from inner and outer contacts of the delay lines.

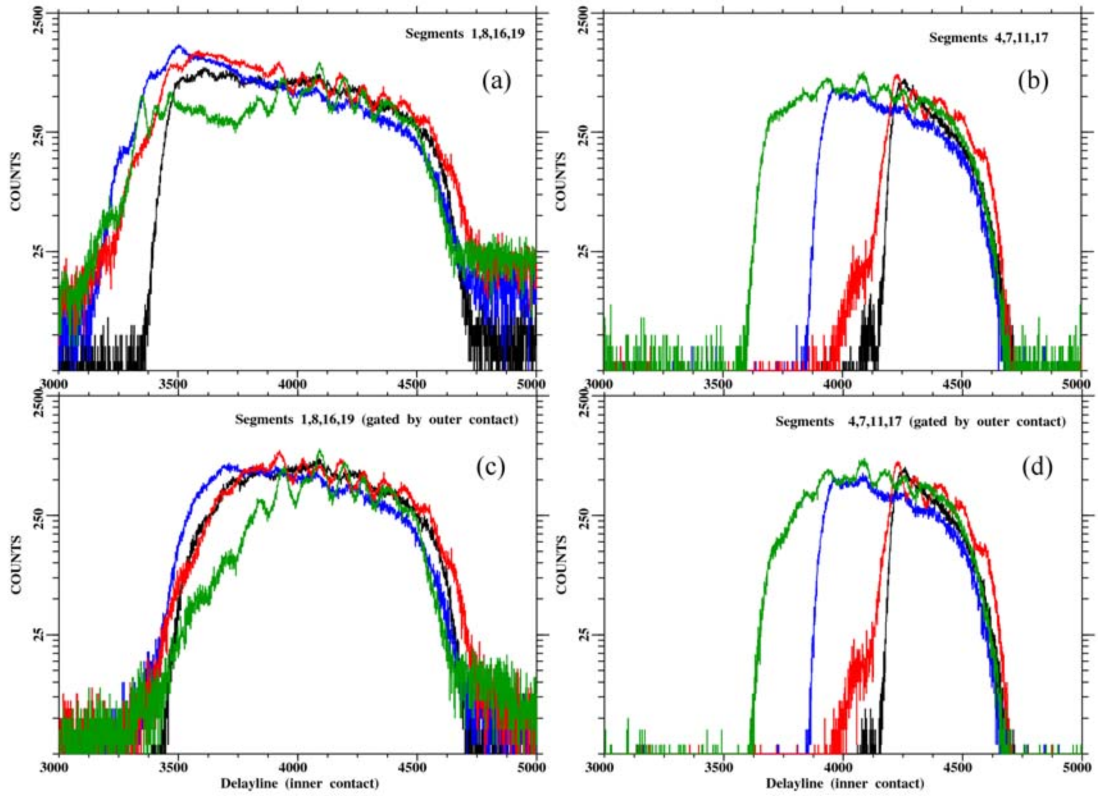

Fig 7. Top panel shows the SDL readout for different PPAC segments: (7a) 1 (black) 8 (blue) 16 (red) 19 (green) and (7b) 4(black) 7(blue) 11 (red) and 17 (green). The corresponding readouts figs 7c, 7d in coincidence with the outer contact are shown in the bottom panel.

The SDL readouts for individual PPAC segments are shown in fig 7a-b (top panel). The bottom panel (7c-d) shows the corresponding readouts gated by a non-zero signal from the outer readout. The following conclusions can be drawn by inspecting these figures. Firstly, the segments having similar count rates in fig 6 show similar delay line spectra. The edges of these spectra are expected to match the geometrical acceptance angle of 15º – 45º in lab. It appears that the segments counting at a lower rate have lower gas gain at forward angles (warped PCB?) and consequently show a truncated position spectrum. Secondly, due to position-dependent attenuation, the readouts from the outer contacts are not sensitive to forward angle data.

From the observed delay line readout, the θ_p of the detected particle can be calculated from the following relationships:

$\tan\theta_p = a \cdot x + b$, where **x** is the time difference t_{inner} - $t_{cathode}$ and the constants a, b are calculated assuming the TAC edges at channels 3400 & 4550 correspond to the angles 15° & 45°.

An independent position spectrum (fig 8) was constructed from the time difference spectra between pairs of delay-line signals ($t_{inner} - t_{outer}$). While the right edge of this spectrum corresponds to $\theta_p \sim 45º$, the angle corresponding to left edge is expected to be considerably larger than the geometrical edge of 15º.

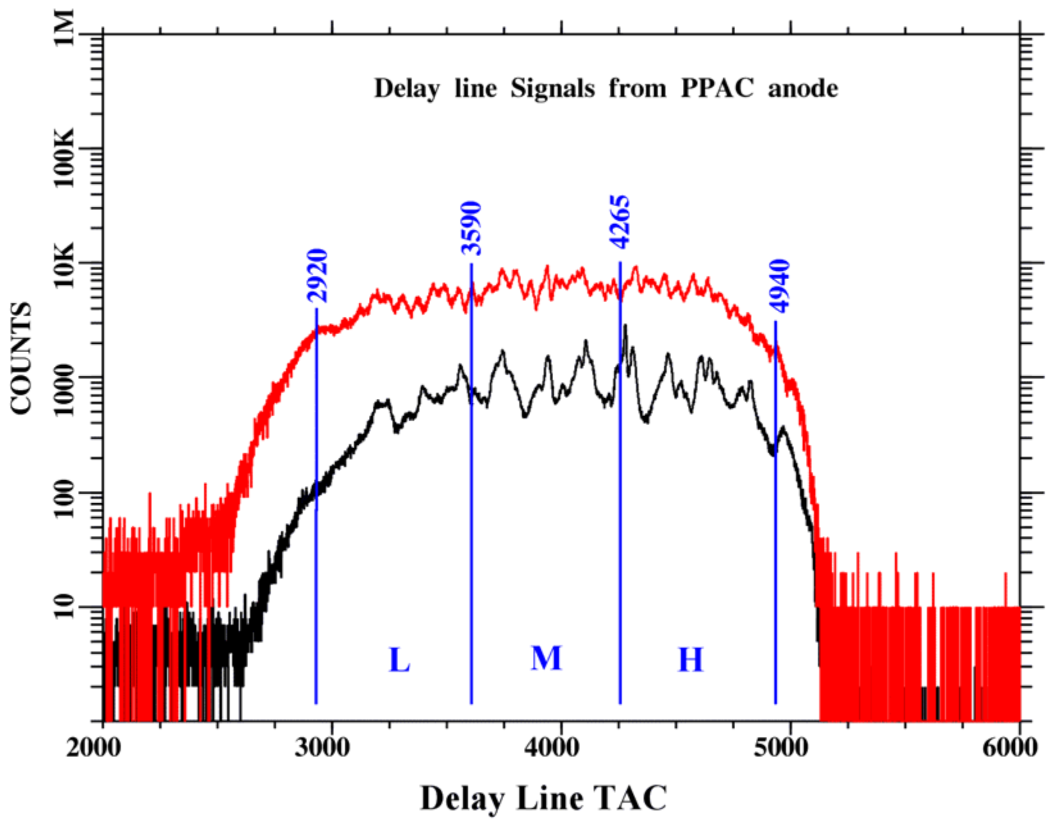

Fig.8: DDL spectra for (i) segments 1-10 (black-bottom) and (ii) segments 11-20 (red-top). The count rates in the two detectors were different as there was no signal from some of the segments

From the DDL readout, the angle of the detected particle can be calculated by using a similar relationship:

$\tan\theta_p = a \cdot y + b$, where **y** is the time difference $t_{inner} - t_{outer}$ .To obtain a calibration for the DDL readout, the total angular range was subdivided into three groups L (channels 2920-3590), M (channels 3590-4265) and H (4265 – 4940). The SDL spectra gated by these three angular regions are shown in fig 9. Using the calibration for SDL readout, the boundaries of the DDL groups corresponds to angles of 21.1º, 28.9º, 36.9º and 43.6º respectively. Using a linear least square fit, the calibration for the DDL readout is found to be:

$$15° \rightarrow \text{channel } 2637;\ \ 45° \rightarrow \text{channel } 5216$$

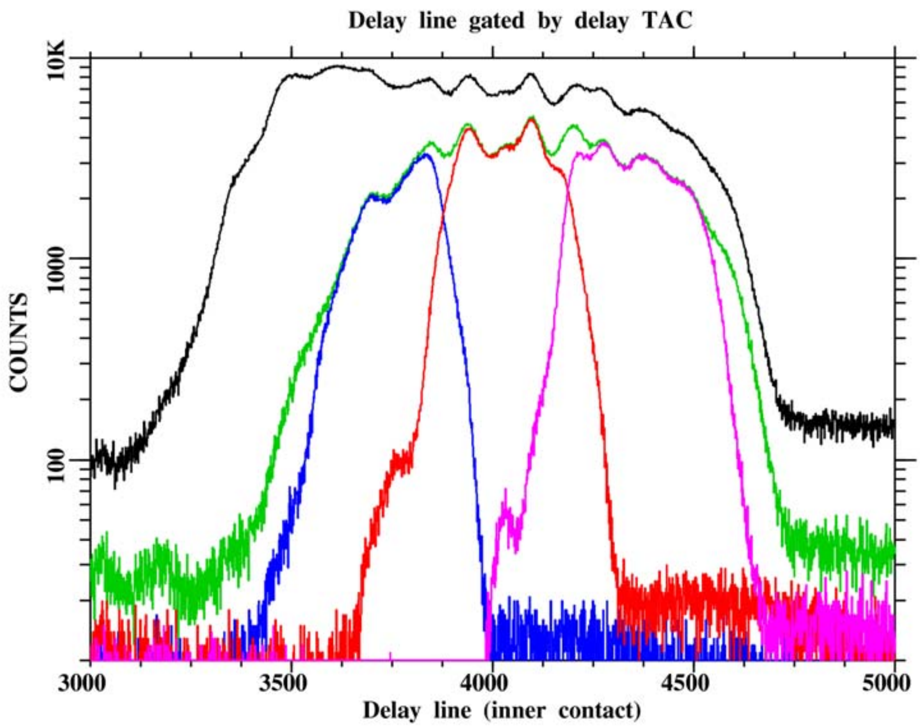

Fig 9. SDL angle readout gated by different regions of DDL (i) black - ungated (ii) green – full DDL range (iii) blue – L (iv) red – M and (v) pink – H region (see text).

The ϕ angle for the detected particle is calculated to be;

ϕ_p **= 18* [K - ξ],** where **K** is the hit segment and ξ is a random number between 0 & 1

From the knowledge of θ_p & ϕ_p, the Doppler correction on the γ-spectra can be calculated event by event. Initial estimates of Doppler correction for the Clover detectors using the nominal values of θ_γ, ϕ_γ for the centre of the detector were not very good, showing prominent tailing at both low and higher energy side (fig.10). The centroids of the Doppler-corrected peaks showed a dependence on PPAC segment, indicating only partial Doppler correction. There was also a shift in peak shape between individual crystals. Although the total area under the Coulomb-excitation peak is not affected by the peak-shape, large systematic error can be introduced in the estimation of the Compton background under a peak if the peak is very broad. It was decided to minimise the peak widths by applying separate Doppler corrections for individual crystals instead of a common correction for the clover as a whole. Readjustment of the calibrations θ_γ, ϕ_γ for individual crystals was carried out to eliminate the residual ϕ_p dependence.

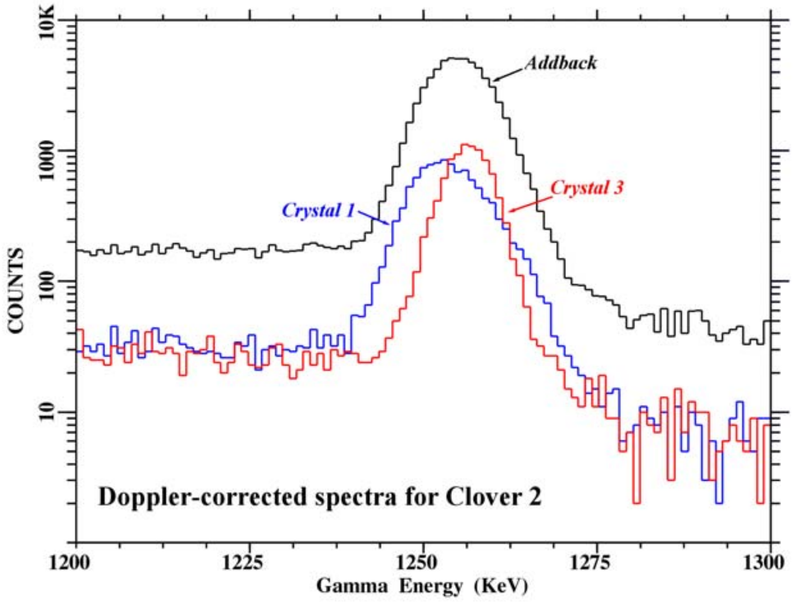

Fig.10: Doppler corrected spectra from individual crystals in Clover # 2 assuming a common correction for the clover as a whole.

Method for improved Doppler Correction

The Doppler shifted γ-energy is given by $\mathbf{E_\gamma \sim E^o_\gamma\ [\ 1 + v/c\ \cos(\Theta_{p\gamma})]}$

with $\mathbf{\cos(\Theta_{p\gamma}) = \cos(\theta_p)\cos(\theta_\gamma) + \sin(\theta_p)\sin(\theta_\gamma)\cos(\phi_p - \phi_\gamma)}$

For a given θ_p and θ_γ, the energy shows a strong dependence on the phase angle $\phi_{p\gamma}$ between the detectors. Since the γ-rays are detected in the backward hemisphere and the projectile-like particles are detected in the forward hemisphere, $(\theta_p + \theta_\gamma) \sim 180°$.

$$\mathbf{E_\gamma^{min} = E_\gamma \sim E^o_\gamma\ [\ 1 + v_p/c\ \cos(\theta_p + \theta_\gamma)]} \qquad \ldots 1$$

$$\mathbf{E_\gamma^{max} = E_\gamma \sim E^o_\gamma\ [\ 1 + v_p/c\ \cos(\theta_p - \theta_\gamma)]} \qquad \ldots 2$$

The minimum value of γ-energy corresponds to when the γ and particle are detected on diametrically opposite side ($\phi_{p\gamma} \sim 180°$) and the maximum value when they are detected on the same side ($\phi_{p\gamma} \sim 0°$). A plot of E_γ vs ϕ_p closely resembles a sine-wave (fig.11):

$$\mathbf{E_\gamma = A + B\cos(\phi_p - \phi_o)}$$

From a least-square fit of the experimental energies with a sine wave, the quantities E_γ^{min}, E_γ^{max} & ϕ_o can be determined**. The phase angle ϕ_γ of the γ-detector corresponds to ϕ_0 for projectile-excitation γ-rays and $(\pi + \phi_0)$ for target-excitation γ-rays.**

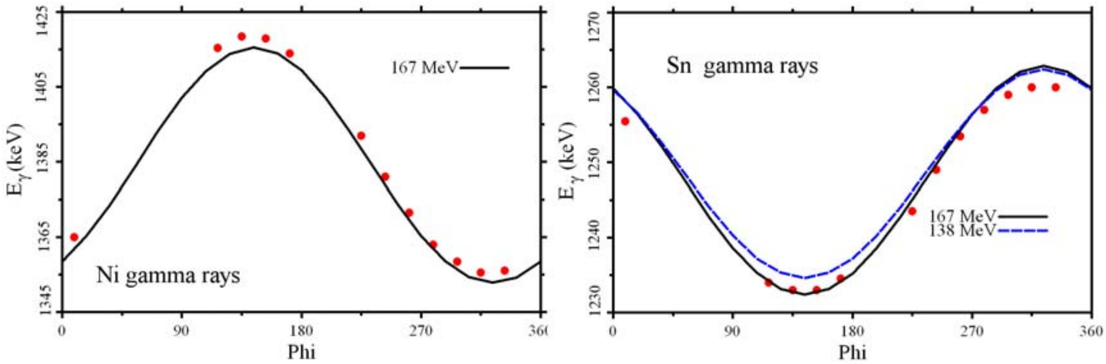

Fig.11: Doppler oscillations for Crystal 1 of Clover 2. The circles are experimental centroids for Ni and Sn peaks for the middle gate in DDL readout. The solid curves correspond to the theoretical predictions for E_B =167 MeV, θ_p = 32.9°, θ_γ = 142.7° & ϕ_γ = 143.2° (see text). For Sn γ-rays, theoretical curves for two different E_B (= 167 & 138 MeV) are shown. (see also Appendix III)

The calculated variation of E_γ^{max} & E_γ^{min} with the detector angle θ_p for different values of θ_γ are shown in fig.12(a-b). The angle difference **($\theta_p - \theta_\gamma$)** can be calculated from E_γ^{max}. The quantity **($\theta_p + \theta_\gamma$)** is however not well determined from E_γ^{min} as cosθ is insensitive to the value of θ for θ ~ 180°. **For γ-rays emitted from projectile-like fragments, unambiguous determination of both θ_p & θ_γ is not possible from the observed Doppler shifts.**

We have tried to extract the geometrical angles θ_γ, ϕ_γ for the clover detectors from the experimental data by analyzing the Doppler shift pattern for each clover crystal as a function of anode segment ϕ_p. The DDL position spectrum range was divided into three bins – **L**ow (L), **M**iddle (M) and **H**igh (H) which nominally corresponded to angular ranges of θ_p ~ 21.1°-28.9°, 28.9°-36.9° and 36.9°-43.6°. For each of the combination, the γ-spectra from a given crystal gated by different ϕ-segments (3 x 4 x 4 x 20 spectra!) were collected and the centroids for the projectile-excitation and target-excitation γ-rays were extracted. The geometrical angles (θ_γ,ϕ_γ) for each clover crystal were adjusted to reproduce the phase and amplitude of oscillation for the Ni peak. Since the lifetimes of the excited states of Ni and Sn populated in the reaction were much larger than the transit times of the beam through the foil, the decay takes place primarily after the beam (and recoils) comes out of the target. The effective beam energy used for Doppler correction of Ni-excitation was reduced to 167 MeV to take into account ~ 8 MeV energy loss in the target. The extracted average θ_γ,ϕ_γ for each crystal are summarised in Table III.

For Sn γ-rays, shown in the right panel of Fig 11, the calculated amplitude of Doppler oscillations are overestimated by about 10% using the values (θ_γ,ϕ_γ) needed to reproduce the same for Ni γ-rays. This difference can be qualitatively understood by incorporating the significant energy loss of the slow moving recoils in the analysis.

The program SHRIM-2008 was used to calculate the specific energy loss of Ni and Sn nuclei in the Sn target. The thickness of the target was taken to be ~ 0.55 mg/cm^2. The average energy loss of the recoils in the target was calculated to be ~ 20% of the initial value.

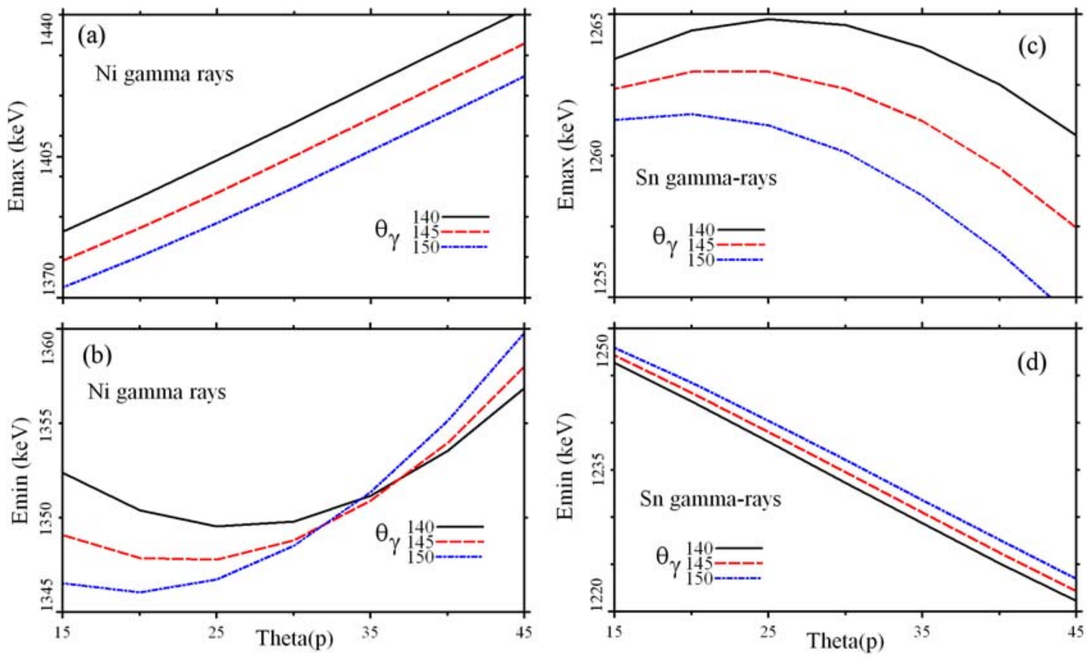

Fig.12: Calculated Doppler-shifted peak positions for projectile- & target-excitation γ-rays as a function of detector angle θ_p. The energy loss in the target has been neglected in the above calculations.

Table III: List of angles θ_γ, ϕ_γ for individual crystals required to reproduce the Doppler shift of Ni peaks

E_B =167 MeV

CLOVER NO	Crystal 1		Crystal 2		Crystal 3		Crystal 4	
	θ_γ	ϕ_γ	θ_γ	ϕ_γ	θ_γ	ϕ_γ	θ_γ	ϕ_γ
1	130.7	53.4	140.3	64.9	146.1	55.5	140.5	43.5
2	142.7	144.2	147.6	124.4	137.0	118.9	133.2	132.9
3	137.1	-33.4	143.8	-46.9	135.3	-56.5	128.8	-44.0
4	144.5	-114.1	138.9	-129.2	128.3	-118.0	135.4	-106.5

In the Doppler correction routine, the effect of reducing the recoil velocity v_R by 10% can be simulated by reducing the effective beam energy E_B by 20% to ~138 MeV (appendix VI). One can use an effective E_B to minimise the width of the Sn Doppler peaks; the total area under the Doppler peak, as expected, is insensitive to its width.

The optimised values of θ_γ, ϕ_γ for individual crystals were used to make Doppler correction for the clover detector as a whole. For γ-events with single hits, the angles for individual crystals were used. For multi-hit γ-events, we used the average angle for all crystals hit. This is a reasonable assumption as computer simulation indicates that double-hit events (which correspond to about 50% of single-hit events) are localised near the common edge of the crystals.

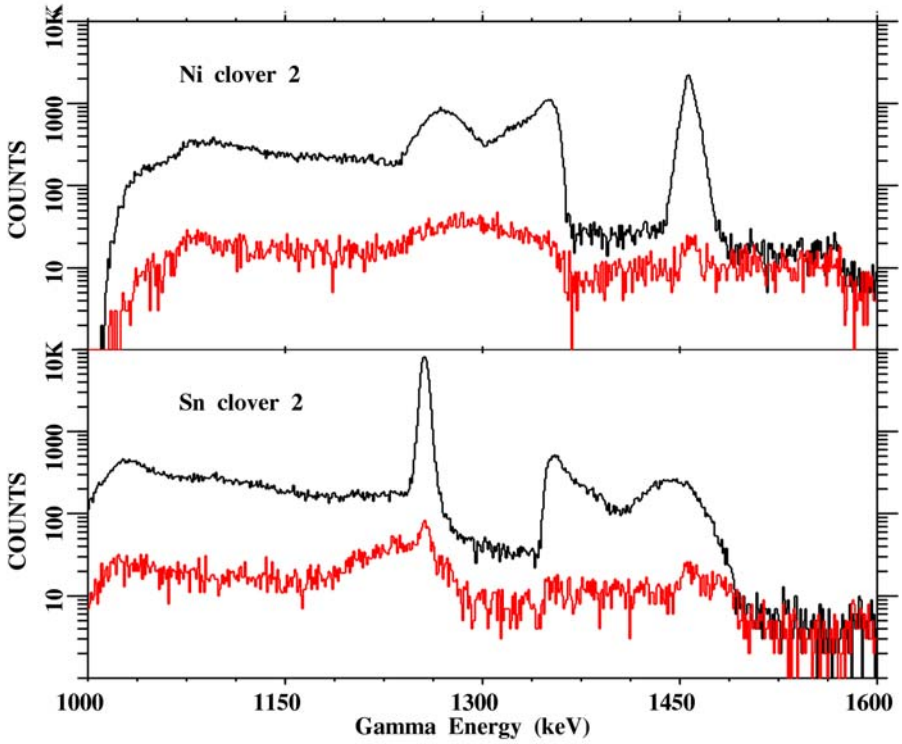

Fig. 13: Doppler corrected add-back spectra for Clover detector #2. The black & red curves correspond to the spectra under 'prompt' and 'random' peaks in Clover-PPAC TOF spectrum. The top and bottom set of curves correspond to Doppler corrections assuming projectile excitation & target excitation

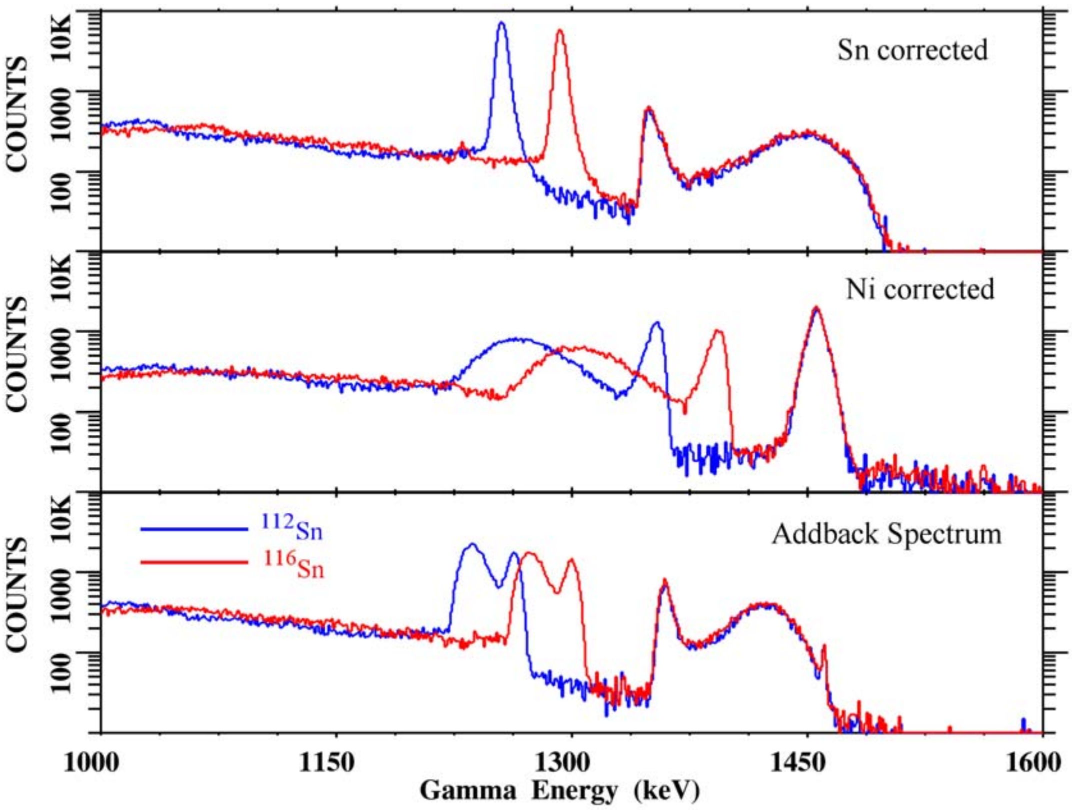

Fig 14. Doppler corrected spectrum for ^{112}Sn (blue) and ^{116}Sn (red) targets

RESULTS

The Doppler-corrected add-back spectra for Coulomb excitation of Ni and Sn are shown in fig.13. For comparison, the random background under each peak is also shown. For extracting the area under a γ-peak, the peak shape was assumed to be Gaussian in nature with exponential tail on both sides. A linear background underneath the peak was assumed. Inspection of Fig 13 shows that major part of the background under the Ni peak arises from the contribution from 'random' events. As a result, removal of a smooth background under a peak, to a large extent, removes the 'random' contribution. Explicit subtraction of the 'random' spectrum from the 'prompt' spectrum would greatly increase the statistical error for the continuum and contribute to an increased error in peak area. Residual peaking in the 'random' spectra was less than 1% of the peak area under 'prompt' peak and has been neglected in the analysis.

We used two independent methods for determination of θ_p event by event for each γ-p coincidence (i) DDL readout which had a reduced background but limited angular acceptance range $\theta_p \sim 21^o$-44^o and (ii) SDL readout having a larger acceptance range of $\theta_p \sim 15^o$-44^o but increased background due to increased random and reduced suppression of Sn-like particles. The Doppler-corrected spectra for ^{112}Sn and ^{116}Sn are shown in fig 13. To reduce systematic errors, identical line shapes were used to extract peak areas under ^{112}Sn excitation (1257 keV) and ^{116}Sn excitation (1294 keV).

Table IVA

Peak areas from DDL analysis

Clover No	^{112}Sn target		^{116}Sn target		^{112}Sn/Ni	^{116}Sn/Ni	^{112}Sn/^{116}Sn
	Sn excitation	Ni excitation	Sn excitation	Ni excitation	ratio	ratio	ratio
1	26237 ± 233	11142 ± 155	21208 ± 224	12129 ± 173	2.355 ± 0.039	1.748 ± 0.031	1.346 ± 0.032
2	59050 ± 349	25093 ± 275	48567 ± 393	27902 ± 297	2.353 ± 0.029	1.741 ± 0.023	1.352 ± 0.025
3	55357 ± 378	23732 ± 247	44573 ±303	25656 ± 283	2.333 ±0.030	1.737 ±0.022	1.343 ±0.024
4*	19488 ±202	8160 ±129	15614 ±180	9124 ±138	2.388 ±0.045	1.711 ±0.032	1.396 ±0.037

** Clover 4 had a drift problem (the ratio ^{112}Sn/^{116}Sn kept on changing from 1.30 to 1.40 during the duration of the experiment) and has been excluded from the final analysis.*

For clover 1 and clover 4, one of the crystals (#2) showed considerable gain drift during the run and has been excluded from the analysis. Crystal 4 of Clover 4 had a much poorer intrinsic resolution (~ 10 keV) compared to the other three (2.5 – 3 keV) and have also been excluded. As a result, the absolute number of counts from detectors 1 & 4 are substantially smaller than those of 2 & 3.

The experimental ^{112}Sn/^{116}Sn ratios, extracted using DDL and SDL readouts are tabulated in table IVA and IVB respectively. Both methods gave very similar results despite covering different angular range. This is discussed in detail at a later section in the context of comparing with theoretical predictions.

Table IVB

Peak areas from SDL analysis

Clover No	^{112}Sn target		^{116}Sn target		^{112}Sn/Ni ratio	^{116}Sn/Ni ratio	^{112}Sn/^{116}Sn ratio
	Sn excitation	Ni excitation	Sn excitation	Ni excitation			
1	30932 ±251	12969 ±204	24496 ±251	13823 ±219	2.385 ±0.043	1.772 ±0.033	1.345 ±0.035
2	69957 ±416	28984 ±330	56421 ±456	31659 ±344	2.413 ±0.031	1.782 ±0.024	1.354 ±0.025
3	65376 ±532	27426 ±363	51903 ±504	29202 ±389	2.383 ±0.037	1.777 ±0.029	1.341 ±0.030
4*	24042 ±240	10025 ±154	19005 ±230	10928 ±161	2.398 ±0.043	1.739 ±0.033	1.379 ±0.036

** Clover 4 had a drift problem (the ratio ^{112}Sn/^{116}Sn kept on changing from 1.30 to 1.40 during the duration of the experiment) and has been excluded from the final analysis.*

The energy resolution of individual ϕ-segments was strongly dependent on the relative phase difference with respect to Clover detectors. The angular distribution of Ni and Sn-like excitations in the laboratory frame were also significantly different. To check the sensitivity of the ^{112}Sn/^{116}Sn ratio to this dependence, we have subdivided the data into two sets (i) $|\phi_{\gamma\text{-PPAC}}| < 90°$ and (ii) $|\phi_{\gamma\text{-PPAC}}| > 90°$. These are shown in fig 15 for Clover#2. The areas under the Sn and Ni peaks are tabulated in table IV. Although the Sn/Ni ratios are sensitive to the range of ϕ-angles selected in the analysis, the overall ratio for ^{112}Sn/^{116}Sn is in-sensitive to the range of ϕ used.

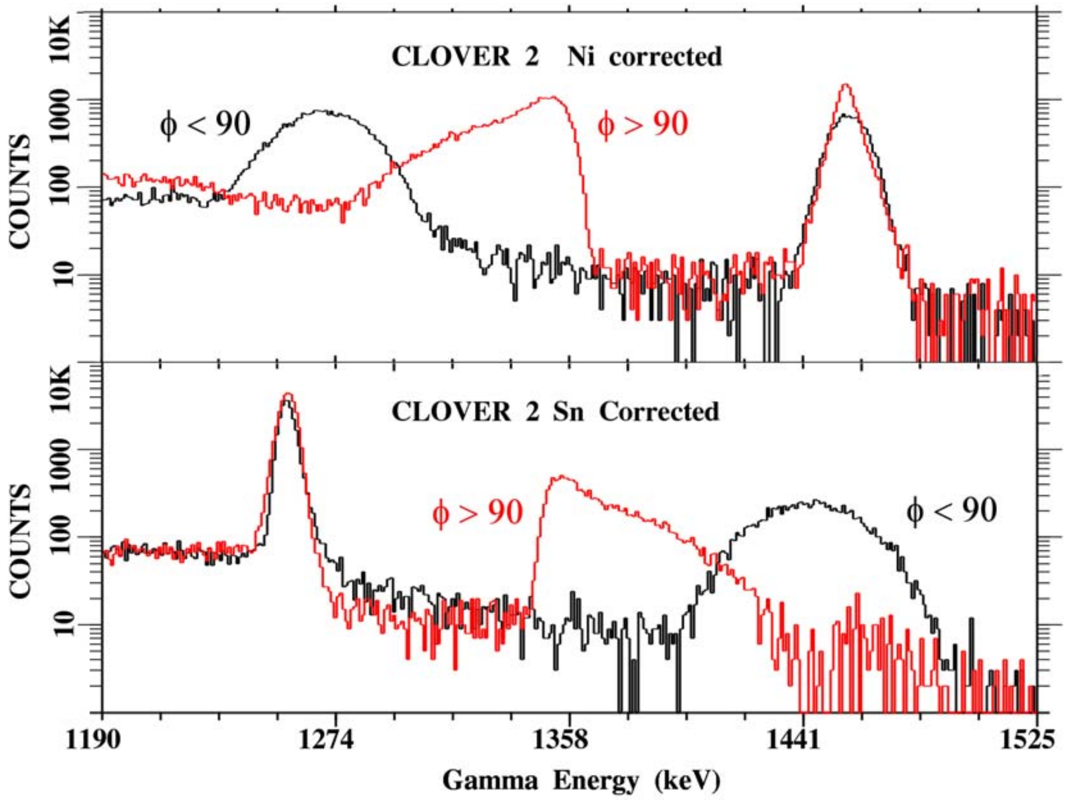

Fig.15: Doppler corrected add-back spectra for Clover detector #2. The black & red curves correspond to the spectra for $-90 < \phi_{\gamma p} < 90$ and $90 < \phi_{\gamma p} < 270$. The top and bottom set of curves correspond to Doppler corrections assuming projectile excitation & target excitation

Table V

φ-dependence of p-γ cross-section (clover 2)

$\phi_{\gamma p}$	^{112}Sn target		^{116}Sn target		^{112}Sn/Ni ratio	^{116}Sn/Ni ratio	^{112}Sn/^{116}Sn ratio
	Sn excitation	Ni excitation	Sn excitation	Ni excitation			
-90 - 90	24993 ±158	10799 ± 208	21040 ± 314	12194 ± 295	2.314 ±0.046	1.725 ±0.049	1.341 ±0.046
90 - 270	33800 ±343	14069 ± 438	27597 ± 260	15377 ± 553	2.402 ±0.078	1.794 ±0.066	1.338 ±0.066

Experimental Angular Dependence of $^{112}Sn/^{116}Sn$ ratio

Theoretical calculations indicate that the yield $\sigma(\theta_p)$ for Coulomb excitation is strongly dependent on the impact parameter and the Q-value of the reaction. Due to the difference in 2^+ excitation energies for ^{112}Sn and ^{116}Sn, the yields would be peaking at different values of θ_p. Consequently, the yield ratio $^{112}Sn/^{116}Sn$ for the same B(E2) value would have an angular dependence, ranging from 1.277 to 1.100 in the angular range 15° - 45°. This introduces an uncertainty in the estimation of 'average' ratio, as the detection efficiency of the PPAC had a dependence on the angular range covered.

An attempt has been made to estimate the angle dependence of the detection efficiency by comparing the measured yield with theoretical predictions. The whole angular range covered by SDL method was subdivided into four bins and the yield as well as $^{112}Sn/^{116}Sn$ ratio determined. For relative normalization between the ^{112}Sn and ^{116}Sn data sets, the *total area* under the Ni peaks was used to extract the double ratio. This exercise was carried out for Clover 2, which had the best timing resolution.

Table VI

Angular Dependence of cross-section (clover 2)

Angular Range θ_p	^{112}Sn target		^{116}Sn target		$^{112}Sn/^{116}Sn$ ratio	Relative weight (w_i)
	Sn excitation	Ni excitation	Sn excitation	Ni excitation		
15-44	69475 ±470	28723 ±317	56033 ±399	31449 ±325	1.358 ±0.024	
15 -21	3367 ±105		2570 ±90		1.434 ±0.070	0.046
21 -29	14357 ±232		11177 ±199		1.406 ±0.040	0.200
29-37	24967 ±244		19846 ±206		1.377 ±0.029	0.356
37-44	26470 ±294		22159 ±277		1.308 ±0.029	0.398

Weighted mean of the four angular ranges is 1.349 ± 0.019 which is consistent with the value for the full angular range of 15-44°. There is very little contribution from the forward angle data due to relatively lower weights associated with it.

For the theoretical computation, the angle integrated ratio is equivalent to the weighted mean for different angles with weights proportional to theoretical yield for ^{116}Sn excitation:

$$\langle \text{Mean ratio} \rangle = \Sigma\ \text{yield(i). ratio(i)}$$

This allows us to directly incorporate the varying detector efficiency by the measured weights w_i tabulated in table VI.

(*need to add a table on estimated detector efficiency as a function of angle)*

Some definitions

Weight for a bin = ^{116}Sn counts in the bin/total count of ^{116}Sn over the whole angular range

Statistical weight for each bin $P_i = w_i$ /error(i)**2

Weights normalised to unity $W_i = P_i/\Sigma P_i$

Statistical Average $\underline{x} = \Sigma W_i x_i$

Statistical error of the average $\underline{\sigma}^2 = \Sigma$ [W_i. error(i)] **2

Agrees with the normal definition if all weights w_i are equal !

SUMMARY

From the weighted average of four measurements (using four clover detectors) The ratio $^{112}Sn/^{116}Sn$ for Coulomb excitation cross-section is given by:

$$\sigma(^{112}Sn)/\sigma(^{116}Sn) = 1.347 \pm 0.015 \quad \text{(DDL analysis)}$$

$$1.348 \pm 0.017 \quad \text{(SDL analysis)}$$

The measured $^{112}Sn/^{116}Sn$ ratio has to be corrected for the difference in efficiency for photopeak energies corresponding to Doppler shifted Coulomb excited peaks from the respective targets. An ^{152}Eu source placed at the target position was used for relative efficiency determination. In the limited energy range 1.0 -1.5 MeV, the efficiency curve can be approximated by an exponential function

$f(E) \sim f_0 \exp(-E/E_0)$ with $E_0 \approx$ 2096,2184,2245 & 2262 keV for detectors 1-4.

Since the difference in the energies of the Doppler shifted peaks is small, the ratio of the two efficiencies can be approximated as:

$$f(^{112}Sn)/f(^{116}Sn) \approx \exp(\Delta E/E_0) \approx 1.017 \pm 0.001$$

$\Delta E \approx (1293.5 - 1256.8)*(1249.0/1256.8) = 36.5$ keV is the shifted energy difference between the two γ-transitions.

The double ratio, **corrected for detector efficiency**, is given by

$$\boldsymbol{\sigma(^{112}Sn)/\sigma(^{116}Sn) = 1.324 \pm 0.015}$$

<u>Correction for isotopic impurity</u>

Isotopic impurity for ^{112}Sn target used	99.5 ± 0.2%
Isotopic purity for ^{116}Sn target	98.0 ± 0.1%

For excitation of Ni, all isotopes of Sn would be equally effective. For target excitation, on the other hand, other isotopes of Sn can be rejected by tight energy selection.

Isotope	^{112}Sn	^{114}Sn	^{116}Sn	^{118}Sn	^{120}Sn
2^+ energy	1257	1300	1293	1230	1171 keV

Except for the pair $^{114,116}Sn$, other γ-rays can be rejected from energy resolution (~ 6 keV after Doppler correction). The amount of ^{114}Sn impurity in ^{116}Sn is reported be less than 0.1%. The measured $^{112}Sn/^{116}Sn$ B(E2) ratios should therefore be reduced by a factor corresponding to the isotopic purity of the targets:

$$(98.0 \pm 0.1\%)/(99.5 \pm 0.2\%) = 0.985 \pm 0.003$$

The final double ratio or cross-sections corrected for detector efficiency & target purity, is given by

$$\underline{\boldsymbol{\sigma(^{112}Sn)/\sigma(^{116}Sn) = 1.305 \pm 0.015}}$$

Coulomb excitation cross sections

Coulomb excitation calculations are performed with FORTRAN program: *lell30e1.f*
input-file: input, output-file: output and anggro.
Cross sections are integrated with FORTRAN program: *anggro.f*
input-file: input and coulex(=anggro see above), output-file: output
(www-linux.gsi.de/~wolle/INDIA)

In a first step the Coulomb excitation cross section (lell30e1.f) is calculated (see appendix VIII). Then we can distinguish 3 cases for the particle-γ angular correlation (anggro.f) (see appendix IX): **(i)** calculation in the rest-frame (I24=1, Q_0=1, Q_2=0, Q_4=0), **(ii)** calculation in the laboratory frame (only Lorentz-boost: I24=0, Q_0=1, Q_2=0, Q_4=0), **(iii)** calculation in the laboratory frame with γ-ray angular correlation (I24=0, Q_0=Q_2=Q_4=1). The results from anggro.f have to be multiplied by 4π to obtain the cross sections in [barn].
First the normalisation was calculated for ^{58}Ni→^{116}Sn at **175MeV**. The nuclear structure data are tabulated in appendix VII and the results are given below for two different angular ranges: $\theta_{lab}=15^0$-45^0 and $\theta_{lab}=21.1^0$-43.7^0.

θ_γ φ_γ	θ_{cm}		**^{116}Sn**: σ_2[mb] ^{58}Ni→^{116}Sn 175MeV	**^{58}Ni**: σ_2[mb] ^{58}Ni→^{116}Sn 175MeV	ratio ^{116}Sn/^{58}Ni
135^0,55^0	22.4^0-65.7^0	**(i)**	60.80	39.77	1.529
		(ii)	59.94	36.46	1.644
		(iii)	61.63	38.26	1.611
	31.5^0-63.9^0	**(i)**	53.09	35.07	1.514
		(ii)	52.34	32.14	1.629
		(iii)	53.80	33.72	1.596

In a second step the cross sections are calculated for ^{58}Ni→^{112}Sn at 175MeV. The nuclear structure data were taken from appendix VII.

θ_γ φ_γ	θ_{cm}		**^{112}Sn**: σ_2[mb] ^{58}Ni→^{112}Sn 175MeV	**^{58}Ni**: σ_2[mb] ^{58}Ni→^{112}Sn 175MeV	ratio ^{112}Sn/^{58}Ni
135^0,55^0	22.7^0-66.5^0	**(i)**	74.88	37.98	1.972
		(ii)	73.78	34.81	2.120
		(iii)	75.78	36.52	2.075
	31.8^0-64.7^0	**(i)**	65.32	33.63	1.942
		(ii)	64.37	30.75	2.093
		(iii)	66.05	32.26	2.047

From both tables the double ratio $^{112}Sn/^{116}Sn$ was determined

$\theta_\gamma\ \varphi_\gamma$	θ_{cm}		ratio $^{112}Sn/^{116}Sn$
135^0,55^0	22.7^0-66.5^0	**(i)**	1.290
		(ii)	1.290
		(iii)	1.288
	31.8^0-64.7^0	**(i)**	1.283
		(ii)	1.285
		(iii)	**1.283**

Since the g-factor of the first excited state in all Sn isotopes is very small (g(2^+)~0), one expects no distortion of the γ-ray angular distribution due to the deorientation effect. Therefore, the calculated double ratio 1.283 was used to determine from the experimental double ratio 1.304±0.024 the B(E2)-value for ^{112}Sn using the following formula: $B(E2,0^+ \rightarrow 2^+) = \frac{1.304}{1.283} \cdot 0.240 = 0.244$ e^2b^2.

Since the B(E2) values are directly proportional to the Coulomb excitation cross sections, the error of the B(E2)-value for ^{112}Sn was determined from the B(E2) ratio

$$\frac{B(E2,0^+ \rightarrow 2^+)_{112-Sn}}{B(E2,0^+ \rightarrow 2^+)_{116-Sn}} = \frac{B(E2,0^+ \rightarrow 2^+)_{112-Sn}}{0.209(6)} = 1.168(22)$$

The error propagation ($df^2 = (x \cdot dy)^2 + (y \cdot dx)^2$) for a product ($f = x \cdot y$) yields the following result

$$B(E2,0^+ \rightarrow 2^+) = 0.244(8)\ \left[e^2b^2\right]$$

In the following table several effects of the theoretical calculations are discussed which may influence the determination of the B(E2)-value for ^{112}Sn

$\theta_\gamma\ \varphi_\gamma$	Θ_{lab}			ratio $^{112}Sn/^{116}Sn$	$B(E2,0^+ \rightarrow 2^+)$ $[e^2b^2]$
135^0,55^0	21.1^0-43.7^0	Isotropic distribution	**(ii)**	1.285	0.244
	15^0-45^0	γ-ray angular distribution	**(iii)**	1.288	0.243
	15^0-45^0	E_{lab}=175MeV		1.291	0.243
	15^0-45^0	E_{lab}=171MeV		1.297	0.241

The last two calculations were performed without taking the γ-ray angular distribution into consideration (using only lell30e1.f). The data are shown in the next table for two bombarding energies, the initial beam energy (175MeV) and the energy of 171MeV taking into account the slowing down in 50% of the target thickness. For ^{58}Ni

projectiles at 175MeV slowed down in a Sn target (0.48mg/cm^2) an energy loss of $\frac{dE}{dx} = 16.4\left[\frac{MeV}{mg/cm^2}\right]$ was calculated.

θ_{cm}	E_{lab}[MeV]	**^{116}Sn**: σ_2[mb] ^{58}Ni→^{116}Sn	**^{58}Ni**: σ_2[mb] ^{58}Ni→^{116}Sn	ratio ^{116}Sn/^{58}Ni	ratio ^{112}Sn/^{116}Sn
22.4^0-65.7^0	175	59.68	39.69	1.504	
22.4^0-65.7^0	171	51.24	33.09	1.549	
		^{112}Sn: σ_2[mb] ^{58}Ni→^{112}Sn	**^{58}Ni**: σ_2[mb] ^{58}Ni→^{112}Sn	ratio ^{112}Sn/^{58}Ni	
22.7^0-66.5^0	175	73.54	37.89	1.941	1.291
22.7^0-66.5^0	171	63.22	31.47	2.009	1.297

A comparison of these effects shows that the analysis is completely insensitive to the γ-ray angular distribution, a different angular range and the energy loss of the projectiles in the Sn target lowers slightly the extracted B(E2) value. **The final B(E2) value for ^{112}Sn**, which includes also the slowing down of 58Ni projectiles in the Sn target, is listed below

$$B(E2, 0^+ \rightarrow 2^+) = 0.242(8) \ \left[e^2 b^2\right]$$

The influence of the higher-lying states (appendix 5) are listed below

θ_{cm}		**^{116}Sn**: σ_2[mb] ^{58}Ni→^{116}Sn 175MeV single excitation	**^{116}Sn**: σ_2[mb] ^{58}Ni→^{116}Sn 175MeV multiple excitation	ratio ^{112}Sn/^{116}Sn 175MeV single (multiple)
22.4^0-65.7^0	(iii)	61.57	62.69 (1.02)	
31.5^0-63.9^0	(iii)	53.74	54.72 1.02)	
		^{112}Sn: σ_2[mb] ^{58}Ni→^{112}Sn 175MeV single excitation	**^{112}Sn**: σ_2[mb] ^{58}Ni→^{112}Sn 175MeV multiple excitation	
22.7^0-66.5^0	(iii)	75.75	76.18 (1.01)	1.230 (1.215)
31.8^0-64.7^0	(iii)	66.02	66.35 (1.01)	1.229 (1.213)

Some more calculations, which are replaced by the following tables with the correct angular ranges:

$\theta_\gamma\ \varphi_\gamma$	θ_{cm}		**^{116}Sn**: σ_2[mb] $^{58}Ni\rightarrow^{116}Sn$ 171MeV	**^{58}Ni**: σ_2[mb] $^{58}Ni\rightarrow^{116}Sn$ 171MeV	ratio $^{116}Sn/^{58}Ni$
$135^0,55^0$	22.4^0-65.7^0	**(i)**	52.21	33.16	1.575
		(ii)	51.47	30.44	1.691
		(iii)	53.16	31.91	1.666
	31.5^0-63.9^0	**(i)**	45.70	29.30	1.560
		(ii)	45.06	26.89	1.676
		(iii)	46.51	28.19	1.650
	31.5^0-44.3^0	**(i)**	12.29	7.182	1.711
		(ii)	12.18	6.511	1.871
		(iii)	12.72	6.914	1.840
	44.3^0-55.1^0	**(i)**	17.00	10.97	1.550
		(ii)	16.76	10.05	1.668
		(iii)	17.32	10.52	1.646
	55.1^0-63.9^0	**(i)**	16.41	11.16	1.470
		(ii)	16.11	10.33	1.560
		(iii)	16.47	10.76	1.531

$\theta_\gamma\ \varphi_\gamma$	θ_{cm}		**^{112}Sn**: σ_2[mb] $^{58}Ni\rightarrow^{112}Sn$ 171MeV	**^{58}Ni**: σ_2[mb] $^{58}Ni\rightarrow^{112}Sn$ 171MeV	ratio $^{112}Sn/^{58}Ni$	ratio $^{112}Sn/^{116}Sn$
$135^0,55^0$	22.7^0-66.5^0	**(i)**	64.38	31.54	2.041	1.296
		(ii)	63.44	28.95	2.191	1.296
		(iii)	65.33	30.37	2.151	1.291
	31.8^0-64.7^0	**(i)**	56.37	27.90	2.020	1.295
		(ii)	55.54	25.60	2.170	1.295
		(iii)	57.20	26.83	2.132	1.292
	31.8^0-44.9^0	**(i)**	15.63	6.927	2.256	1.319
		(ii)	15.49	6.282	2.466	1.318
		(iii)	16.14	6.672	2.419	1.315
	44.9^0-55.7^0	**(i)**	20.63	10.30	2.003	1.292
		(ii)	20.35	9.441	2.156	1.292
		(iii)	20.96	9.882	2.121	1.289
	55.7^0-64.7^0	**(i)**	20.09	10.67	1.883	1.281
		(ii)	19.69	9.882	1.993	1.277
		(iii)	20.09	10.28	1.954	1.277

Final calculations with the correct angular range:

$\theta_\gamma\ \varphi_\gamma$	θ_{cm}		^{116}**Sn**: σ_2[mb] $^{58}Ni \rightarrow ^{116}Sn$ 171MeV	^{58}**Ni**: σ_2[mb] $^{58}Ni \rightarrow ^{116}Sn$ 171MeV	ratio $^{116}Sn/^{58}Ni$
$135^0,55^0$	22.4^0-65.7^0	**(i)**	52.20	33.16	1.574
		(ii)	51.47	30.44	1.691
		(iii)	53.16	31.91	1.666
	31.9^0-65.7^0	**(i)**	48.97	31.60	1.550
		(ii)	48.25	29.03	1.662
		(iii)	49.75	30.41	1.636
	31.9^0-44.2^0	**(i)**	11.92	6.978	1.708
		(ii)	11.82	6.326	1.869
		(iii)	12.34	6.718	1.837
	44.2^0-55.1^0	**(i)**	17.13	11.05	1.550
		(ii)	16.90	10.12	1.670
		(iii)	17.44	10.60	1.645
	55.1^0-65.7^0	**(i)**	19.92	13.58	1.467
		(ii)	19.53	12.58	1.553
		(iii)	19.96	13.08	1.526

$\theta_\gamma\ \varphi_\gamma$	θ_{cm}		^{112}**Sn**: σ_2[mb] $^{58}Ni \rightarrow ^{112}Sn$ 171MeV	^{58}**Ni**: σ_2[mb] $^{58}Ni \rightarrow ^{112}Sn$ 171MeV	ratio $^{112}Sn/^{58}Ni$	ratio $^{112}Sn/^{116}Sn$
$135^0,55^0$	22.7^0-66.5^0	**(i)**	64.38	31.54	2.041	1.297
		(ii)	63.44	28.95	2.191	1.296
		(iii)	65.33	30.37	2.151	1.291
	32.3^0-66.5^0	**(i)**	60.17	30.02	2.004	1.293
		(ii)	59.25	27.58	2.148	1.293
		(iii)	60.96	28.89	2.110	**1.290**
	32.3^0-44.7^0	**(i)**	15.94	6.628	2.405	1.408
		(ii)	14.80	6.009	2.463	1.318
		(iii)	15.42	6.383	2.416	1.315
	44.7^0-55.7^0	**(i)**	20.96	10.46	2.004	1.293
		(ii)	20.67	9.583	2.157	1.292
		(iii)	21.30	10.03	2.124	1.291
	55.7^0-66.5^0	**(i)**	24.25	12.93	1.876	1.278
		(ii)	23.76	12.00	1.980	1.275
		(iii)	24.23	12.48	1.942	1.272

Based on the new angular range of 21.4^0-45^0 in the laboratory frame the final B(E2) value for ^{112}Sn, which includes also the slowing down of ^{58}Ni projectiles in the Sn target, is listed below

$$B(E2, 0^+ \rightarrow 2^+) = 0.243(8)\ \left[e^2b^2\right]$$

Calculation of Coulomb Excitation Cross-section

To calculate the Coulomb excitation cross-section for a given B(E2) matrix element, the program lell30e1.f from http://www-linux.gsi.de/~wolle/INDIA/ was used. The input parameters were taken from input.txt with the following modifications :

Input

Target Mass: 112 or 116

Target Excitation: 1.257 or 1.2935

Projectile Excitation : 1454 keV

LAB angle = 30.0 (change card 20 → 20. 30.)

Matrix element = 0.490 for both targets.

The calculated theoretical cross-sections in barn are:

For ^{112}Sn,

Target Ex: Theta(cm)=45.09 Recoil angle= 67.08 $d\sigma/d\Omega_L$ = 0.05053

Projectile Ex: Theta(cm)=45.10 Recoil angle= 67.01 $d\sigma/d\Omega_L$ = 0.02751

^{112}Sn/Ni ratio: 1.8368

For ^{116}Sn,

Target Ex: Theta(cm)=44.56 Recoil Angle = 67.33 $d\sigma/d\Omega_L$ = 0.04711

Projectile Ex: Theta(cm)=44.57 Recoil Angle = 67.28 $d\sigma/d\Omega_L$ = 0.02868

^{116}Sn/Ni ratio= 1.6426

Due to the difference in centre of mass energies, Ni excitation yield would be different for the two targets. This has to be corrected !

For identical matrix elements, the double ratio of Coulomb excitation cross-sections

^{112}Sn/^{116}Sn ratio (theoretical)= 1.118

Major part of this ratio comes from the change in excitation energies of the two nuclei. The kinematic effects, seen for Ni excitation, are cancelled out in the double ratio. The 4% increase for Ni excitation between the two targets is expected as the c.m. energy is higher for the heavier target which more than compensates for the reduction in c.m. angle.

The effect of change in excitation energy alone is comparable to E_γ^5 ratio (1.15) for the 2+ states of ^{112,116}Sn.

The final results are:

[B(E2) ^{112}Sn] / [B(E2) ^{116}Sn] = 1.166 ± 0.022

This can be compared with the earlier measurement of B(E2) ratio for $^{112,116}Sn$ as

$$(240\pm14)/(209\pm7) = 1.148 \pm 0.075$$

There is one source of theoretical uncertainty that we have ignored in the analysis. The angular distribution for coulomb-excitation cross-section, apart from the dependence on incident energy, is also sensitive to the Q-value of the reaction; higher Q-value would shift the angular distribution to higher c.m. angle. This can be easily seen in the calculated angular distributions for projectile and target. This would affect the double ratio of the phase-space factor to ~ ± 2% level over the angular range in view of the difference in excitation energies of $^{112,116}Sn$.

Table V shows the calculated Coulomb excitation cross-sections in mb/sr^2 unit and the double-ratio. Last two rows show the angle integrated cross-sections ($\Sigma \sin\theta\ \sigma(\theta)$) in the angular ranges 15°-45° & 20°-40° respectively. Considering the uncertainty in the accepted angular range, theoretical double ratio for coulomb excitation probability is given by **1.124 ± 0.005**

Table V

Coulomb excitation cross-section (mb/sr^2)

Scattering angle (Lab)	^{112}Sn target		^{116}Sn target		^{112}Sn/Ni ratio	^{116}Sn/Ni ratio	**^{112}Sn/^{116}Sn Ratio**
	Sn excitation	Ni excitation	Sn excitation	Ni excitation			
15.0	11.61	3.743	9.523	3.921	3.102	2.429	**1.277**
20.0	28.75	12.47	25.31	12.98	2.305	1.945	**1.183**
25.0	42.85	21.35	38.89	22.29	2.007	1.745	**1.150**
30.0	50.56	27.51	47.11	28.68	1.838	1.643	**1.119**
35.0	52.66	30.17	49.56	31.65	1.745	1.566	**1.115**
40.0	50.94	30.34	48.40	31.84	1.679	1.520	**1.105**
45.0	47.07	28.74	45.05	30.25	1.638	1.489	**1.100**
50.0	42.21	26.19	40.64	27.65	1.611	1.470	**1.097**
15.0 - 45.0	**152.46**	**85.14**	**142.50**	**89.22**	**1.791**	**1.597**	**1.121**
20.0 – 40.0	**116.2**	**63.85**	**108.18**	**66.82**	**1.819**	**1.619**	**1.124**

Appendix I:

Generating clover-PPAC time difference spectrum

1. Reject multi-hit events in PPAC
2. Reject zero events in Clover 2 TAC
3. Generate Clover-2 add-back energy spectrum (with energy gate?)
4. Copy ADC42 to ADC16 (to put Clover time before PPAC time)
5. Define TDC command between ADC16-36
6. *New TAC is between Clover 2 (any segment) & any of the PPAC detectors (ADC17-36)
7. Project this TAC with different Clover-2 energies

* *For getting the best time resolution, the centroids for each of the gamma-PPAC spectra are first matched for instrumental delays. To avoid variations in the timings for individual clover segments, TAC spectra were gated by individual Clover segments. The timing spreads between individual Clover segments were ~ ns for 1 MeV gamma rays To simplify centroid matching, a condition of non-zero delayline signal was incorporated to eliminate the left-side peak associated with the detection of Sn-particles..*

Appendix II:

Configuration file for Clover#1 for generating Doppler correction

```
  0# ADC NUMBER#  44 PRESORT_OPTION#   0
! CONFIG commands last modified on  14/01/2009 !
! inputs for CUBE and TRIPLE modified  PPAC USER added
! remove crystal with poor resolution
  1# SHIFT DEST-ADC#   2 FROM-ADC#   2 SCALE-CONSTANT#   3 VALUE#  0.0000E+00
      OFFSET-CONSTANT#   4 VALUE#  0.0000E+00
! select clover 1 timing adc to be non-zero
  2# CONDITION #   1 GATING-ADC#  41 LOWER-LIMIT#   100 UPPER-LIMIT#  4000
  3# CNOT COND#   2  =.NOT.COND#   1
  4# IFCON     #   2 GOTO#    0 INSTRUCTION# 200#
 ! add-back foir clover 1
  5# CLOVER 1st_of_4_ADC#     1 TDC#    41 DEST_ADC#    51
     BITMAP_ADC#    52 Threshold_in_keV#    20.0 keV_per_channel#   1.000
     !   LOW-T-CUTOFF#  100 HIGH-T-CUTOFF# 4000
  6# PROJ  COND#   0 SPECTRUM#   51 ADC#  51 ISHL#   0 1-D=  1#
  7# PROJ  COND#   0 SPECTRUM#   52 ADC#  52 ISHL#   0 1-D=  2#
! selects energy region 1 -2 MeV in Clover
  8# CONDITION #   3 GATING-ADC#  51 LOWER-LIMIT#  1000 UPPER-LIMIT#  2000
  9# CNOT COND#   4  =.NOT.COND#   3
 10# IFCON     #   4 GOTO#    0 INSTRUCTION# 200#
!  calculate which PPAC segment has fired
 11# PPAC   MAP_ADC#   53 TAC_ADC#  54 Max_no_of_Bits#  20
    FIRST_TDC#  17 LOWER_LIMIT#   200 UPPER_LIMIT#   730
 12# PROJ  COND#   0 SPECTRUM#   53 ADC#  53 ISHL#   0 1-D=  3#
! remove multiple hits in PPAC
 13# CONDITION #   5 GATING-ADC#  53 LOWER-LIMIT#     1 UPPER-LIMIT#    20
 14# CNOT COND#   6  =.NOT.COND#   5
 15# IFCON     #   6 GOTO#    0 INSTRUCTION# 200#
 ! calculate time difference between left & right delay-line counters
 16# TDC DEST-TAC#  55 OFFSET#  4096 TDCMAP#  56 ! &  57
     ADC# FOR-FIRST-TDC#  37 ADC# FOR-LAST-TDC#  40
     LOW-TIME-CUTOFF#   100 HIGH-TIME-CUTOFF#  4000
 17# PROJ  COND#   0 SPECTRUM#   54 ADC#  55 ISHL#   0 1-D=  4#
! valid events are timing from both sides of top & bottom delay line counter
 18# CONDITION #   3 GATING-ADC#  56 LOWER-LIMIT#     3 UPPER-LIMIT#     3
 19# CONDITION #   4 GATING-ADC#  56 LOWER-LIMIT#    12 UPPER-LIMIT#    12
 20# COR   COND#   5 COMPOSED-OF#   3   4   0
 21# CNOT COND#   6  =.NOT.COND#   5
 22# IFCON     #   6 GOTO#    0 INSTRUCTION# 200#
!
! select the accepted angular range in particle detector
!
 23# CONDITION #   7 GATING-ADC#  55 LOWER-LIMIT#  2920 UPPER-LIMIT#  4940
 24# CNOT COND#   8  =.NOT.COND#   7
 25# IFCON     #   8 GOTO#    0 INSTRUCTION# 200#
! calculate TOF between clover & PPAC
 26# SHIFT DEST-ADC#  16 FROM-ADC#  41 SCALE-CONSTANT#   1 VALUE#
1.0000E+00
      OFFSET-CONSTANT#   2 VALUE#  0.0000E+00
 27# TDC DEST-TAC#  58 OFFSET#  4096 TDCMAP#  59 ! &  60
     ADC# FOR-FIRST-TDC#  16 ADC# FOR-LAST-TDC#  36
     LOW-TIME-CUTOFF#   100 HIGH-TIME-CUTOFF#  4000
 28# CONDITION #   1 GATING-ADC#  58 LOWER-LIMIT#  4350 UPPER-LIMIT#  5950
 29# CNOT COND#   2  =.NOT.COND#   1
 30# IFCON     #   2 GOTO#    0 INSTRUCTION# 200#
```

```
! project all spectra for 'good' events
  31# PROJ  COND#   0 SPECTRUM#   55 ADC#  51 ISHL#   0 1-D=  5#
  32# PROJ  COND#   0 SPECTRUM#   56 ADC#  52 ISHL#   0 1-D=  6#
  33# PROJ  COND#   0 SPECTRUM#   57 ADC#  53 ISHL#   0 1-D=  7#
  34# PROJ  COND#   0 SPECTRUM#   58 ADC#  55 ISHL#   0 1-D=  8#
  35# PROJ  COND#   0 SPECTRUM#   59 ADC#  56 ISHL#   0 1-D=  9#
  36# PROJ  COND#   0 SPECTRUM#   60 ADC#  58 ISHL#   0 1-D= 10#
! calculate Doppler correction assuming projectile or target excitation ( projectile detected)
  37# USER-CALL ! Doppler correction for GSI experiment
     Projectile#   58. Target#  112. Beam_Energy_in_MeV#     175.
     segment_1# Theta_Gamma#   136.30 Phi_gamma#    53.40
     segment_2# Theta_Gamma#   140.10 Phi_gamma#    64.90
     segment_3# Theta_Gamma#   149.20 Phi_gamma#    55.50
     segment_4# Theta_Gamma#   143.30 Phi_gamma#    43.50
     chnl_no_for_15deg#    2362. chnl_no_for_45deg#    5552.
     Theta_ADC#   55 Phi_ADC#   53 Clover_ADC#   51 Clover_bitmap#   52
     Projectile_Exc_ADC#   61 Target_Exc_ADC#     62 Cutoff#  1000.0
! gate on 'prompt' & 'random' events
  38# CONDITION #  31 GATING-ADC#  58 LOWER-LIMIT#  4750 UPPER-LIMIT#  5550
  39# CONDITION #  32 GATING-ADC#  58 LOWER-LIMIT#  4350 UPPER-LIMIT#  4750
  40# CONDITION #  33 GATING-ADC#  58 LOWER-LIMIT#  5550 UPPER-LIMIT#  5950
  41# COR   COND#  34 COMPOSED-OF#  32  33   0
  42# PROJ  COND#  31 SPECTRUM#  103 ADC#  61 ISHL#   0 1-D= 11#
  43# PROJ  COND#  34 SPECTRUM#  104 ADC#  61 ISHL#   0 1-D= 12#
  44# PROJ  COND#  31 SPECTRUM#  105 ADC#  62 ISHL#   0 1-D= 13#
  45# PROJ  COND#  34 SPECTRUM#  106 ADC#  62 ISHL#   0 1-D= 14#
! subtract spectrum 104 from 103 offline to get 'true prompts'
! this is done later on the sorted spectra
  46# END-DIALOGUE
```

Appendix III:

$^{58}Ni \rightarrow ^{112}Sn$, E=175MeV, $\vartheta_p = 32.3^0$, $\vartheta_\gamma = 147.0^0$, $\varphi_\gamma = 143.2^0$

^{58}Ni measured with PPAC, ^{58}Ni excited

$$v_{cm} = 0.04634 \cdot \left(1 + \frac{A_2}{A_1}\right)^{-1} \cdot \sqrt{\frac{E}{A_1}} = 0.02746$$

$$\theta_{cm} = \vartheta_1 + \arcsin\left(\frac{A_1}{A_2}\right) \cdot \sin\vartheta_1 = 48.4^0$$

$$v_1 = v_{cm} \cdot \left\{1 + \left(\frac{A_2}{A_1}\right)^2 + 2 \cdot \left(\frac{A_2}{A_1}\right) \cdot \cos\theta_{cm}\right\}^{1/2} = 0.07417$$

$$\cos\vartheta_{\gamma 1} = \cos\vartheta_\gamma \cdot \cos\vartheta_1 + \sin\vartheta_\gamma \cdot \sin\vartheta_1 \cdot \cos(\varphi_\gamma - \varphi_1)$$

$$\cos(\varphi_\gamma - \varphi_1) = \cos\varphi_\gamma \cdot \cos\varphi_1 + \sin\varphi_\gamma \cdot \sin\varphi_1$$

$$\frac{E_{\gamma 0}}{E_\gamma} = \frac{1 - v_1 \cdot \cos\vartheta_{\gamma 1}}{\sqrt{1 - v_1^2}}$$

$\varphi_1\ [^0]$	$\cos\vartheta_{\gamma 1}$	$E_\gamma \equiv E_\gamma^{\min}[keV]$
9	-0.9118	1358
27	-0.8374	1365
45	-0.7504	1374
63	-0.6594	1382
81	-0.5732	1391
99	-0.5003	1398
117	-0.4478	1403
135	-0.4208	1406
153	-0.4221	1406
171	-0.4515	1403
189	-0.5060	1398
207	-0.5804	1390
225	-0.6674	1382
243	-0.7584	1373
261	-0.8446	1365
279	-0.9175	1358
297	-0.9700	1353
315	-0.9969	1350
333	-0.9957	1350
351	-0.9663	1353

^{112}Sn measured with PPAC, ^{58}Ni excited

$$v_{cm} = 0.04634 \cdot \left(1 + \frac{A_2}{A_1}\right)^{-1} \cdot \sqrt{\frac{E}{A_1}} = 0.02746$$

$$\cos\vartheta_1 = \frac{v_{cm}}{v_1}\left(1 + \frac{A_2}{A_1} \cdot \cos\theta_{cm}\right) \quad with\ \ \theta_{cm} = 180^0 - 2 \cdot \vartheta_2 = 115.4^0$$

$$v_1 = v_{cm} \cdot \left\{1 + \left(\frac{A_2}{A_1}\right)^2 + 2 \cdot \left(\frac{A_2}{A_1}\right) \cdot \cos\theta_{cm}\right\}^{1/2} = 0.04814$$

$$\cos\vartheta_{\gamma 1} = \cos\vartheta_\gamma \cdot \cos\vartheta_1 - \sin\vartheta_\gamma \cdot \sin\vartheta_1 \cdot \cos(\varphi_\gamma - \varphi_2) \quad with\ \ \vartheta_1 = 84.4^0$$

$$\cos(\varphi_\gamma - \varphi_2) = \cos\varphi_\gamma \cdot \cos\varphi_2 + \sin\varphi_\gamma \cdot \sin\varphi_2$$

$$\frac{E_{\gamma 0}}{E_\gamma} = \frac{1 - v_1 \cdot \cos\vartheta_{\gamma 1}}{\sqrt{1 - v_1^2}}$$

$\varphi_2\,(\varphi_1)\ [^0]$	$\cos\vartheta_{\gamma 1}$	$E_\gamma \equiv E_\gamma^{\max}[keV]$
9(189)	-0.4597	1421
27(207)	-0.3212	1430
45(225)	-0.1592	1441
63(243)	0.0104	1453
81(261)	0.1710	1464
99(279)	0.3068	1474
117(297)	0.4045	1481
135(315)	0.4547	1485
153(333)	0.4523	1485
171(351)	0.3976	1481
189(9)	0.2961	1473
207(27)	0.1575	1463
225(45)	-0.0045	1452
243(63)	-0.1741	1440
261(81)	-0.2246	1429
279(99)	-0.4704	1420
297(117)	-0.5682	1414
315(135)	-0.6183	1410
333(153)	-0.6160	1410
351(171)	-0.5613	1414

^{58}Ni→^{112}Sn, E=175MeV, $\vartheta_p = 32.3^0$, $\vartheta_\gamma = 147.0^0$, $\varphi_\gamma = 143.2^0$

^{112}Sn measured with PPAC, ^{112}Sn excited

$$v_{cm} = 0.04634 \cdot \left(1 + \frac{A_2}{A_1}\right)^{-1} \cdot \sqrt{\frac{E}{A_1}} = 0.02746$$

$$v_2 = 2 \cdot v_{cm} \cdot \cos\vartheta_2 = 0.04643$$

$$\cos\vartheta_{\gamma 2} = \cos\vartheta_\gamma \cdot \cos\vartheta_2 + \sin\vartheta_\gamma \cdot \sin\vartheta_2 \cdot \cos(\varphi_\gamma - \varphi_2)$$

$$\cos(\varphi_\gamma - \varphi_2) = \cos\varphi_\gamma \cdot \cos\varphi_2 + \sin\varphi_\gamma \cdot \sin\varphi_2$$

$$\frac{E_{\gamma 0}}{E_\gamma} = \frac{1 - v_2 \cdot \cos\vartheta_{\gamma 2}}{\sqrt{1 - v_2^2}}$$

φ_2 $[^0]$	$\cos\vartheta_{\gamma 2}$	$E_\gamma \equiv E_\gamma^{\min}[keV]$
9	-0.9118	1205
27	-0.8374	1209
45	-0.7504	1213
63	-0.6594	1218
81	-0.5732	1223
99	-0.5003	1227
117	-0.4478	1230
135	-0.4208	1232
153	-0.4221	1232
171	-0.4515	1230
189	-0.5060	1227
207	-0.5804	1223
225	-0.6674	1218
243	-0.7584	1213
261	-0.8446	1208
279	-0.9175	1204
297	-0.9700	1202
315	-0.9969	1200
333	-0.9957	1200
351	-0.9663	1202

^{58}Ni measured with PPAC, ^{112}Sn excited

$$v_{cm} = 0.04634 \cdot \left(1 + \frac{A_2}{A_1}\right)^{-1} \cdot \sqrt{\frac{E}{A_1}} = 0.02746$$

$$\vartheta_2 = 0.5 \cdot (180^0 - \theta_{cm}) \ \textit{with} \ \theta_{cm} = \vartheta_1 + \arcsin\left(\frac{A_1}{A_2} \cdot \sin\vartheta_1\right) = 48.4^0$$

$$v_2 = 2 \cdot v_{cm} \cdot \cos\vartheta_2 = 0.02250 \ \textit{with} \ \vartheta_2 = 65.8^0$$

$$\cos\vartheta_{\gamma 2} = \cos\vartheta_\gamma \cdot \cos\vartheta_2 - \sin\vartheta_\gamma \cdot \sin\vartheta_2 \cdot \cos(\varphi_\gamma - \varphi_1)$$

$$\cos(\varphi_\gamma - \varphi_1) = \cos\varphi_\gamma \cdot \cos\varphi_1 + \sin\varphi_\gamma \cdot \sin\varphi_1$$

$$\frac{E_{\gamma 0}}{E_\gamma} = \frac{1 - v_2 \cdot \cos\vartheta_{\gamma 2}}{\sqrt{1 - v_2^2}}$$

$\varphi_1(\varphi_2)$ $[^0]$	$\cos\vartheta_{\gamma 2}$	$E_\gamma \equiv E_\gamma^{\max}[keV]$
9(189)	0.0025	1257
27(207)	-0.1245	1253
45(225)	-0.2729	1249
63(243)	-0.4283	1245
81(261)	-0.5755	1241
99(279)	-0.6999	1237
117(297)	-0.7895	1235
135(315)	-0.8355	1233
153(333)	-0.8333	1234
171(351)	-0.7832	1235
189(9)	-0.6901	1237
207(27)	-0.5631	1241
225(45)	-0.4146	1245
243(63)	-0.2592	1249
261(81)	-0.1121	1254
279(99)	0.0124	1257
297(117)	0.1019	1260
315(135)	0.1479	1261
333(153)	0.1457	1261
351(171)	0.0956	1259

APPENDIX IV :
Range –energy table for Sn on Sn

==

Calculation using SRIM-2006
SRIM version ---> SRIM-2008.04
Calc. date ---> March 14, 2009

==

Disk File Name = SRIM Outputs\Tin in Tin

Ion = Tin [50] , Mass = 119.902 amu

Target Density = 7.2816E+00 g/cm3 = 3.6939E+22 atoms/cm3
======= Target Composition ========

Atom Name	Atom Numb	Atomic Percent	Mass Percent
----	----	-------	-------
Sn	50	100.00	100.00

====================================

Bragg Correction = 0.00%
Stopping Units = MeV / (mg/cm2)
See bottom of Table for other Stopping units

Ion Energy	dE/dx Elec.	dE/dx Nuclear	Projected Range	Longitudinal Straggling	Lateral Straggling
-----------	----------	----------	----------	----------	----------
1.00 MeV	1.118E+00	3.234E+00	2357 A	1001 A	698 A
1.10 MeV	1.182E+00	3.151E+00	2600 A	1088 A	761 A
1.20 MeV	1.242E+00	3.071E+00	2846 A	1173 A	823 A
1.30 MeV	1.297E+00	2.996E+00	3095 A	1258 A	886 A
1.40 MeV	1.348E+00	2.924E+00	3347 A	1342 A	949 A
1.50 MeV	1.397E+00	2.857E+00	3601 A	1425 A	1011 A
1.60 MeV	1.442E+00	2.792E+00	3857 A	1507 A	1074 A
1.70 MeV	1.486E+00	2.731E+00	4116 A	1589 A	1137 A
1.80 MeV	1.529E+00	2.673E+00	4376 A	1670 A	1200 A
2.00 MeV	1.611E+00	2.565E+00	4904 A	1830 A	1326 A
2.25 MeV	1.709E+00	2.444E+00	5572 A	2025 A	1485 A
2.50 MeV	1.807E+00	2.335E+00	6249 A	2216 A	1644 A
2.75 MeV	1.906E+00	2.237E+00	6931 A	2401 A	1802 A
3.00 MeV	2.005E+00	2.149E+00	7616 A	2580 A	1961 A
3.25 MeV	2.107E+00	2.068E+00	8302 A	2754 A	2118 A
3.50 MeV	2.211E+00	1.994E+00	8988 A	2922 A	2273 A
3.75 MeV	2.317E+00	1.926E+00	9672 A	3084 A	2427 A
4.00 MeV	2.426E+00	1.863E+00	1.04 um	3239 A	2579 A
4.50 MeV	2.650E+00	1.751E+00	1.17 um	3533 A	2876 A
5.00 MeV	2.881E+00	1.654E+00	1.30 um	3804 A	3162 A
5.50 MeV	3.118E+00	1.569E+00	1.43 um	4053 A	3435 A
6.00 MeV	3.361E+00	1.493E+00	1.56 um	4282 A	3695 A

6.50 MeV	3.606E+00	1.425E+00	1.68 um	4491 A	3942 A
7.00 MeV	3.854E+00	1.364E+00	1.80 um	4683 A	4175 A
8.00 MeV	4.352E+00	1.259E+00	2.02 um	5026 A	4605 A
9.00 MeV	4.847E+00	1.171E+00	2.23 um	5317 A	4990 A
10.00 MeV	5.334E+00	1.096E+00	2.43 um	5566 A	5333 A
11.00 MeV	5.809E+00	1.031E+00	2.62 um	5782 A	5642 A
12.00 MeV	6.270E+00	9.741E-01	2.80 um	5971 A	5921 A
13.00 MeV	6.715E+00	9.242E-01	2.97 um	6137 A	6174 A
14.00 MeV	7.144E+00	8.797E-01	3.13 um	6285 A	6405 A
15.00 MeV	7.556E+00	8.399E-01	3.29 um	6417 A	6616 A
16.00 MeV	7.953E+00	8.040E-01	3.44 um	6536 A	6810 A
17.00 MeV	8.334E+00	7.714E-01	3.58 um	6643 A	6990 A
18.00 MeV	8.700E+00	7.416E-01	3.72 um	6742 A	7157 A
20.00 MeV	9.391E+00	6.893E-01	3.99 um	6919 A	7458 A
22.50 MeV	1.018E+01	6.345E-01	4.30 um	7108 A	7785 A
25.00 MeV	1.091E+01	5.886E-01	4.60 um	7267 A	8068 A
27.50 MeV	1.158E+01	5.496E-01	4.88 um	7404 A	8317 A
30.00 MeV	1.220E+01	5.160E-01	5.15 um	7523 A	8540 A
32.50 MeV	1.278E+01	4.866E-01	5.40 um	7628 A	8740 A
35.00 MeV	1.333E+01	4.608E-01	5.65 um	7721 A	8921 A
37.50 MeV	1.385E+01	4.378E-01	5.89 um	7805 A	9087 A
40.00 MeV	1.435E+01	4.173E-01	6.12 um	7881 A	9240 A

Multiply Stopping by	for Stopping Units
7.2814E+01	eV / Angstrom
7.2814E+02	keV / micron
7.2814E+02	MeV / mm
1.0000E+00	keV / (ug/cm2)
1.0000E+00	MeV / (mg/cm2)
1.0000E+03	keV / (mg/cm2)
1.9712E+02	eV / (1E15 atoms/cm2)
9.6617E-02	L.S.S. reduced units

==

Appendix V: Nuclear Structure Data

isotope	I^{π} energy(MeV)	$I_i \rightarrow I_f$ $B(E2;I_i \rightarrow I_f)$	$<I_f//M(E2)//I_i>$ eb	τ (ps)
^{112}Sn	2_1^+ 1.257	$0_1^+ \rightarrow 2_1^+$ 0.240(14)	0.490(14)	0.542(52)
	2_2^+ 2.151	$0_1^+ \rightarrow 2_2^+$ 0.0007(2)	0.026(4)	
		$2_1^+ \rightarrow 2_2^+$ 0.037(15)	0.430(80)	
	0_2^+ 2.191			
	4_1^+ 2.248	$2_1^+ \rightarrow 4_1^+$ 0.032(5)	0.403(32)	
^{116}Sn	2_1^+ 1.294	$0_1^+ \rightarrow 2_1^+$ 0.209(6)	0.457(7)	0.538(15)
	2_2^+ 2.112	$0_1^+ \rightarrow 2_2^+$ 0.0011(4)	0.032(6)	
		$2_1^+ \rightarrow 2_2^+$ 0.013(5)	0.255(45)	
	4_1^+ 2.391	$2_1^+ \rightarrow 4_1^+$ 0.137(25)	0.827(73)	
		$2_2^+ \rightarrow 4_1^+$ 0.360(72)	1.342(128)	
^{120}Sn	2_1^+ 1.171	$0_1^+ \rightarrow 2_1^+$ 0.202(4)	0.449(4)	0.918(18)
^{58}Ni	2_1^+ 1.454	$0_1^+ \rightarrow 2_1^+$ 0.0705(18)	0.266(3)	0.891(22)
		$0_1^+ \rightarrow 2_1^+$ 0.0493(18)	0.222(4)	
	4_1^+ 2.459	$2_1^+ \rightarrow 4_1^+$ 0.0264(24)	0.363(17)	

see: N.-G. Jonsson et al. Nucl.Phys. A371(1981), 333

lifetime of the 2^+ state:

$$\tau[s] = \left\{ [1+\alpha_T(E2)] \cdot 1.225 \cdot 10^{13} \cdot E_\gamma [MeV]^5 \cdot B(E2;2^+ \rightarrow 0^+) [e^2 b^2] \right\}^{-1}$$

relation between B(E2)-values:

$$B(E2;2^+ \rightarrow 0^+) = \frac{1}{5} \cdot B(E2;0^+ \rightarrow 2^+)$$

reduced matrix elements:

$$B(E2;0^+ \rightarrow 2^+) = \langle 2^+ \| M(E2) \| 0^+ \rangle^2$$

isotope	I^{π} energy(MeV)	$I_i \rightarrow I_f$ $B(E3;I_i \rightarrow I_f)$	$<I_f//M(E3)//I_i>$ eb
^{112}Sn	3_1^- 2.355	$0_1^+ \rightarrow 3_1^-$ 0.087(12)	0.295(20)
^{116}Sn	3_1^- 2.266	$0_1^+ \rightarrow 3_1^-$ 0.127(17)	0.356(24)

Appendix VI: Input Data for Coulomb Excitation-Program lell30e1.f

data card #	parameter	input describtion
1	NMAX	number of nuclear states
2	NCM	index of level for which the lab-transformation is done
3	NTIME	-
4	XIMAX	largest number for ξ-parameter
5	EMMAX1	largest magnetic quantum number considered
6	ACCUR	absolute accuracy to which the final probabilities should be computed
	QPAR	effect of the giant dipole resonance
7	OUXI	print-out of ξ-matrix
8	OUPSI	print-out of ψ-matrix
9	OUAMP	print-out of excitation amplitudes
10	OUPROW	print-out of excitation probability during integration
11	OUANG0	print-out of angular distribution coefficients α^0
12	OUANG1	print-out of angular distribution coefficients α^1
13	OUANG2	print-out of angular distribution coefficients α^2
14	OUANG3	print-out of angular distribution coefficients α^3
15	NCORR	-
16	INTERV	number of integration steps
17	Z1	charge number of the projectile
	A1	mass of projectile [amu]
18	Z2	charge number of the target nucleus
	A2	mass of target nucleus [amu]
19	EP	laboratory energy of projectile [MeV]
20	TLBDG	deflection angle [degree] in the lab-system
21	THETA	deflection angle [degree] in the cm-system
22	N	index of level
	SPIN(N)	spin quantum number of the Nth nuclear state
	EN(N)	excitation energy of the Nth nuclear state
	IPAR(N)	parity (-1 neg, 1 pos) of the Nth nuclear state
23	N	index of level
	M	index of level ($M \geq N$)
	ME(N,M,LA)	electric matrix element
	LA	multipolarity ($1 \leq LA \leq 6$)
0		starts the calculation
500		stops the calculation

Appendix VII: Input Data for Angular Distribution-Program anggro.f

data card #	parameter	input describtion
1	I11	output of the conversion coefficients (E2,M1,E1,E3)
	I12	possible decays of a state
	I13	HN (lifetime of the state)
	I14	G_K(N,M)
	I15	F_K(N,M)
	I16	$\alpha^3(k,\kappa)$+feeding
	I17	Spin(N),Spin(M),W(N,K)
	I18	Spin(N),Spin(M),DS(N,K)
	I19	γ-ray angular distribution $\theta_\gamma=0^0,180^0,5^0$ $\varphi_\gamma=0^0$ and 180^0
	I20	-
	I21	excitation probabilities, cross sections, $\alpha^3(k,\kappa)$
	I22	1≡solid angle correction, 2≡ +deorientation, 3≡ +SB
	I23	input M1-matrix element + M1 conversion coefficient
	I24	1≡calc. in rest system, >1 input of θ_γ, φ_γ in rest system
	I25	projectile excitation
2	NCCK	number of values given for K-conversion
	NCCL	number of values given for L-conversion
	NCCM	number of values given for M-conversion
3-5	CCE1	lowest tabulated energy to be interpolated, -1.0 for L,M
	CCE2	lowest tabulated energy of the K, L2, M5 subshell
	CCMIN	min. energy given in the conversion table
	CCMAX	max. energy given in the conversion table
6_1-	α_K,I=1,NCCK	conversion coefficients (K-shell)
7_1-	α_L,I=1,NCCL	conversion coefficients (L-shell)
8_1-	α_M,I=1,NCCM	conversion coefficients (M-shell)
9	IXYZ	I23=1 IXYZ=initial state
	JXYZ	I23=1 JXYZ=final state
	MM1(IXYZ,JXYZ))	I23=1 M1-matrix element (IXYZ→JXYZ)
10	TT	θ_γ
	VGAMMA	φ_γ
	VI1	φ_1
	VI2	φ_γ
	K1LAB	state for cm to lab transformation
11	Q_0,Q_2,Q_4	I22=1 solid angle correction for Ge-detector
		I22=2, I22=3, I22=4, I22=5 (see program)
12	MZahl	number of theta integrations
	NORM	normalization, neg. value ≡ Rutherford
13	XA	initial scattering angle in cm system for integration
	XE	final scattering angle in cm system for integration

Appendix VIII: Important Formulas

nuclear lifetime:

$$\tau[s]=\left\{\sum_M\sum_L\delta^2_{N\to M}(L)\cdot[1+\alpha_{N\to M}(L)]\right\}^{-1}$$

with

$$\delta^2_{N\to M}(E2)\left[s^{-1}\right]=1.225\cdot10^{13}\cdot E_\gamma[MeV]^5\cdot B(E2;I_N\to I_M)\left[e^2b^2\right]$$

$$\delta^2_{N\to M}(M1)\left[s^{-1}\right]=1.758\cdot10^{13}\cdot E_\gamma[MeV]^3\cdot B(M1;I_N\to I_M)\left[\frac{e\hbar}{2m_pc}\right]^2$$

$$\delta^2_{N\to M}(E1)\left[s^{-1}\right]=1.590\cdot10^{17}\cdot E_\gamma[MeV]^3\cdot B(E1;I_N\to I_M)[eb]$$

$$\delta^2_{N\to M}(E3)\left[s^{-1}\right]=5.709\cdot10^{8}\cdot E_\gamma[MeV]^7\cdot B(E3;I_N\to I_M)\left[e^3b^3\right]$$

relation between B(E2) values:

$$B(EL;I_N\to I_M)=\frac{2\cdot I_M+1}{2\cdot I_N+1}\cdot B(EL;I_M\to I_N)$$

reduced matrix element

$$B(EL;I_M\to I_N)=\frac{1}{2\cdot I_M+1}\cdot\left\langle I_N\|M(EL)\|I_M\right\rangle^2$$

Coulomb excitation cross section (single state excitation):

$$\boldsymbol{\sigma_{E2}}=4.918\cdot(1+A_1/A_2)^{-2}\cdot\frac{A_1}{Z_2^2}\cdot\left(E_{MeV}-(1+A_1/A_2)\cdot\Delta E_{MeV}\right)\cdot \mathbf{B(E2;0^+\to2^+)}\cdot f_{E2}(\xi)$$

with

$$\xi=\frac{Z_1\cdot Z_2\cdot A_1^{1/2}\cdot\Delta E'_{MeV}}{12.65\cdot\left(E_{MeV}-0.5\cdot\Delta E'_{MeV}\right)^{3/2}}\quad with\quad \Delta E'_{MeV}=(1+A_1/A_2)\cdot\Delta E_{MeV}$$

!! Functional form of f_{E2} ??